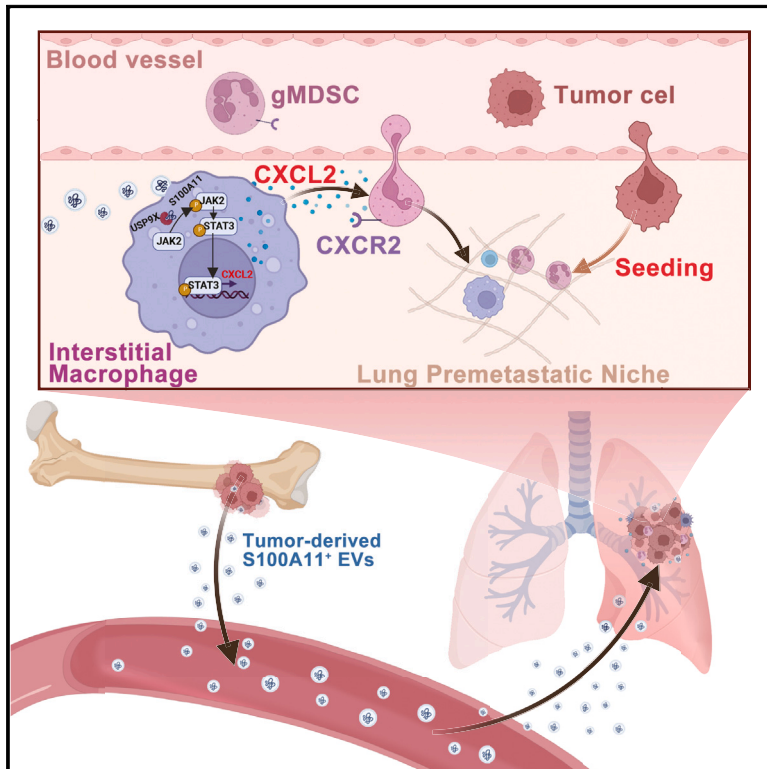Article

Extracellular-vesicle-packaged S100A11 from osteosarcoma cells mediates lung premetastatic niche formation by recruiting gMDSCs

Graphical abstract

Authors

Chuangzhong Deng, Yanyang Xu, Hongmin Chen, ..., Ranyi Liu, Qinglian Tang, Jin Wang

Correspondence

tangql@sysucc.org.cn (Q.T.), wangjinr@sysucc.org.cn (J.W.)

In brief

The interaction between osteosarcoma cells and the lung microenvironment during metastatic progression is not precisely characterized. Deng et al. show that gMDSCs are critical for lung premetastatic niche formation in osteosarcoma. Mechanistically, extracellular-vesicle-packaged S100A11 activates lung macrophages to recruit gMDSCs via CXCL2-CXCR2.

Highlights

- Granulocytic myeloid-derived suppressor cells (gMDSCs) establish lung premetastatic niche

- Osteosarcoma-cell-EV-derived S100A11 induces CXCL2 secretion in lung interstitial macrophages

- Activated macrophages recruit gMDSCs via CXCL2-CXCR2 signal

- High gMDSC level predicts lung metastasis in osteosarcoma

CellPress

Cell Reports

Article

Extracellular-vesicle-packaged S100A11 from osteosarcoma cells mediates lung premetastatic niche formation by recruiting gMDSCs

Chuangzhong Deng,[1,2,4] Yanyang Xu,[1,2,4] Hongmin Chen,[1,2,4] Xiaojun Zhu,[1,2] Lihua Huang,[2,3] Zhihao Chen,[1,2] Huaiyuan Xu,[1,2] Guohui Song,[1,2] Jinchang Lu,[1,2] Wenlin Huang,[2] Ranyi Liu,[2] Qinglian Tang,[1,2,*] and Jin Wang[1,2,5,*]

[1]Department of Musculoskeletal Oncology, Sun Yat-sen University Cancer Center, Guangzhou 510060, P.R. China
[2]State Key Laboratory of Oncology in Southern China, Guangdong Provincial Clinical Research Center for Cancer, Sun Yat-sen University Cancer Center, Guangzhou 510060, P.R. China
[3]Administration Department of Nosocomial Infection, Sun Yat-sen University Cancer Center, Guangzhou 510060, P.R. China
[4]These authors contributed equally
[5]Lead contact
*Correspondence: tangql@sysucc.org.cn (Q.T.), wangjinr@sysucc.org.cn (J.W.)
https://doi.org/10.1016/j.celrep.2024.113751

SUMMARY

The premetastatic niche (PMN) contributes to lung-specific metastatic tropism in osteosarcoma. However, the crosstalk between primary tumor cells and lung stromal cells is not clearly defined. Here, we dissect the composition of immune cells in the lung PMN and identify granulocytic myeloid-derived suppressor cell (gMDSC) infiltration as positively associated with immunosuppressive PMN formation and tumor cell colonization. Osteosarcoma-cell-derived extracellular vesicles (EVs) activate lung interstitial macrophages to initiate the influx of gMDSCs via secretion of the chemokine CXCL2. Proteomic profiling of EVs reveals that EV-packaged S100A11 stimulates the Janus kinase 2/signal transducer and activator of transcription 3 signaling pathway in macrophages by interacting with USP9X. High level of S100A11 expression or circulating gMDSCs correlates with the presentation of lung metastasis and poor prognosis in osteosarcoma patients. In summary, we identify a key role of tumor-derived EVs in lung PMN formation, providing potential strategies for monitoring or preventing lung metastasis in osteosarcoma.

INTRODUCTION

Osteosarcoma is the most common primary cancer of bone and tends to occur in children and adolescents. The 5-year survival rate can reach nearly 70% in patients with localized disease and plummet to less than 20% in patients with metastatic disease.[1] The most common metastatic site is the lung, which is also the primary determinant of prognosis in osteosarcoma patients.[2,3] The underlying mechanisms that mediate lung tropism of osteosarcoma cells remain poorly explored.

Metastasis is a multistep and sophisticated process in which the metastatic microenvironment plays a vital role.[4] Metastasis-initiating cells arriving at the distant site depend on a favorable microenvironment to grow efficiently.[5,6] Primary tumor cells secrete systemic factors that reprogram immune cells, nonimmune stromal cells, and the extracellular matrix at distant organ sites before and during metastasis.[7] The specialized microenvironment established before the formation of clinically detectable metastatic lesions is termed the premetastatic niche (PMN).[8] PMNs support the colonization of tumor cells and ultimately foster the formation of metastatic lesions.

Among tumor-secreted factors, tumor-derived extracellular vesicles (EVs) play a crucial role in establishing the PMN and driving organ tropism of metastasis.[9] EVs are lipid-membrane-enwrapped subcellular particles ranging from 50 nm to several microns that mediate intercellular communication by transferring their bioactive cargos, including DNA, RNA, and protein.[10,11] Accumulating evidence has revealed the multifunctional role of tumor-derived EVs in modulating the immune system, remodeling the extracellular matrix, and inducing angiogenesis or lymphangiogenesis, which together support tumor metastasis.[12,13]

Here, we dissected the composition of immune cells that constitute the lung PMN of osteosarcoma and further explored the role of tumor-derived EVs during this process. We showed that granulocytic myeloid-derived suppressor cells (gMDSCs) significantly accumulated in the lung PMN of an osteosarcoma orthotopic model. Mechanistically, osteosarcoma-cell-derived EVs activated lung interstitial macrophages and induced the expression of CXCL2, which recruited gMDSCs to the lung PMN. Moreover, S100A11, identified in EVs, stimulated the JAK2/STAT3 pathway in macrophages and accounted for the expression of CXCL2. Our work provides new insight into the molecular mechanism by which osteosarcoma-cell-derived EVs reprogram the immune microenvironment in the lung PMN to promote lung metastasis.

RESULTS

gMDSCs infiltrate premetastatic lungs

We first set out to determine the different phases of lung metastasis using an orthotopic spontaneous metastasis model of osteosarcoma using murine K7M2 cells. Lung metastasis was dynamically monitored through *in vivo* bioluminescence imaging and lung H&E staining at the indicated times. In addition, detection of the luciferase gene by RT-PCR was used to confirm the presence of K7M2-luc (luciferase labeled K7M2) cells in the mouse lung. In accordance with previous findings,[14] lung metastasis could be detected 3 weeks after orthotopic inoculation of osteosarcoma cells (Figures S1A–S1C). We also tested the sensitivity of RT-PCR, which was able to detect 10^3 osteosarcoma cells in a lung (Figure S1D). Based on this, we defined week 1 to week 2 as the premetastatic phase of osteosarcoma (Figure S1E). Enlargement of the spleen was observed in tumor-bearing mice during the premetastatic phase (Figure S1F).

Next, we compared the expression profile between normal and premetastatic lungs by RNA sequencing (RNA-seq) (Figure S1G). Of note, Ptp4a1, the top-ranked upregulated gene, was a well-known oncogene, which suggested pro-metastatic transformation in the premetastatic lung microenvironment. In addition, the expression of prometastatic genes, including *S100a8*, *S100a9*, and *Mmp9*, was significantly increased in the lung PMN (Figure 1A). To dissect the composition of the lung PMN of osteosarcoma, we performed flow cytometry analysis of infiltrating immune cells in the lung PMN. The gating strategy is shown in Figure S2. CD4$^+$ T cells were the most abundant cell type, and their abundance remained unchanged in the premetastatic phase. However, both the percentage and overall number of CD11b$^+$Ly6G$^+$ gMDSCs increased markedly (Figure 1B). Subtype analysis showed that gMDSCs, but not mMDSCs (monocytic MDSCs, CD11b$^+$Ly6C^{high}), were the subtype that expanded in the lung PMN (Figures 1C and S3A). Notably, gMDSC accumulation was also observed in the mouse spleen, indicating their systemic mobilization in osteosarcoma-bearing mice (Figure 1C). Immunofluorescence analysis of Ly6G confirmed the accumulation of gMDSCs during lung metastasis formation and localization within metastatic lesions of osteosarcoma (Figures 1D and 1E). In addition, more gMDSCs infiltrated the lung metastatic lesion than the primary bone tumor in both K7M2-bearing mice and osteosarcoma patients (Figures 1F, S3B, and S3C). We further investigated the relationship of peripheral gMDSC numbers with lung metastasis and clinical outcomes in a cohort of osteosarcoma patients. Patients who presented with or developed lung metastasis at 1 year had higher numbers of gMDSCs but not mMDSCs (Figures 1G and S3D). Reduced lung metastasis-free survival was found in osteosarcoma patients with higher levels of gMDSCs (Figure 1H). In accordance with previous reports,[15] gMDSCs isolated from the lung PMN were typically polymorphonuclear and could dramatically suppress the proliferation of both CD4$^+$ and CD8$^+$ T cells (Figures S3E–S3G). These results suggest that gMDSCs may contribute to the generation of an immunosuppressive PMN and promote lung metastasis in osteosarcoma.

gMDSCs mediate lung metastasis by promoting osteosarcoma colonization

Given the abundant infiltration of gMDSCs in the lung PMN, we next investigated the function of gMDSCs in promoting lung metastasis of osteosarcoma cells. To this end, an anti-Ly6G blocking antibody was used to deplete gMDSCs *in vivo*. The expression of prometastatic genes in the lung PMN decreased as a consequence of gMDSC depletion (Figure 2A). Remarkably, depletion of gMDSCs inhibited spontaneous lung metastasis of osteosarcoma with no effect on the growth of primary tumors (Figures 2B and 2C). Moreover, anti-Ly6G treatment significantly reduced the infiltrated number of Ly6G$^+$ gMDSCs and CD4 and CD8 T cells (Figure 2D). To further illustrate that the recruited gMDSCs are responsible for the metastasis of osteosarcoma, we isolated gMDSCs from the premetastatic lungs of K7M2 tumor-bearing mice. The harvested gMDSCs were intravenously injected into other mice, and *ex vivo* imaging showed that infused gMDSCs mainly accumulated in the lungs (Figure S3H). Of note, transplantation of gMDSCs significantly promoted the lung metastasis of K7 cells, a syngenic cell line of K7M2 cells with a poorer ability to metastasize (Figures 2E–2G). Colonization at distant organs is the rate-limiting step of the metastatic process, which underlies the importance of the PMN.[16] We performed a lung colonization assay to explore the functional contribution of gMDSCs to metastasis (Figure 2H). Notably, the colonization of GFP$^+$ osteosarcoma cells in the lungs was significantly reduced in gMDSC-depleted mice (Figures 2I and 2J). Concomitantly, the TUNEL staining assay revealed that the apoptosis rate of colonized tumor cells was much higher in gMDSC-depleted mice (Figure 2J). Together, these results indicate that the accumulation of gMDSCs contributed to the formation of the lung PMN and the promotion of lung colonization by osteosarcoma cells.

Osteosarcoma-cell-derived EVs initiate lung PMN formation

Tumor-derived EVs play a vital role in mediating tumor cell-stromal cell communication and PMN establishment.[9] We therefore probed whether osteosarcoma-cell-derived EVs mediate the accumulation of gMDSCs in the lung PMN. The morphology, diameter, and biomarkers of the isolated EVs were evaluated by electron microscopy (Figure S4A), nanoparticle tracking analysis (Figure S4B), and western blotting (Figure S4C), respectively. As shown in Figure 3A, K7M2-EV-treated mice had more gMDSCs infiltrating the lungs. Moreover, increased expression of gMDSC-related genes (*Arg1* and *Nos2*) was observed after K7M2-EV treatment (Figure 3B). Subsequently, we found that K7M2-EVs significantly promoted lung metastasis of K7 cells (Figures 3C and 3D). Rab27a has been reported to play an essential role in EV secretion.[17] Knocking down Rab27a expression in osteosarcoma cells reduced EV production by nearly 53%, based on NTA analysis (Figure 3E). *In vitro* experiments showed no effect on the invasion and proliferation ability of osteosarcoma cells (Figure S4D and S4E). As expected, inhibition of EV secretion greatly reduced the number of spontaneous lung metastases (Figures 3F and 3G). In addition, knocking down
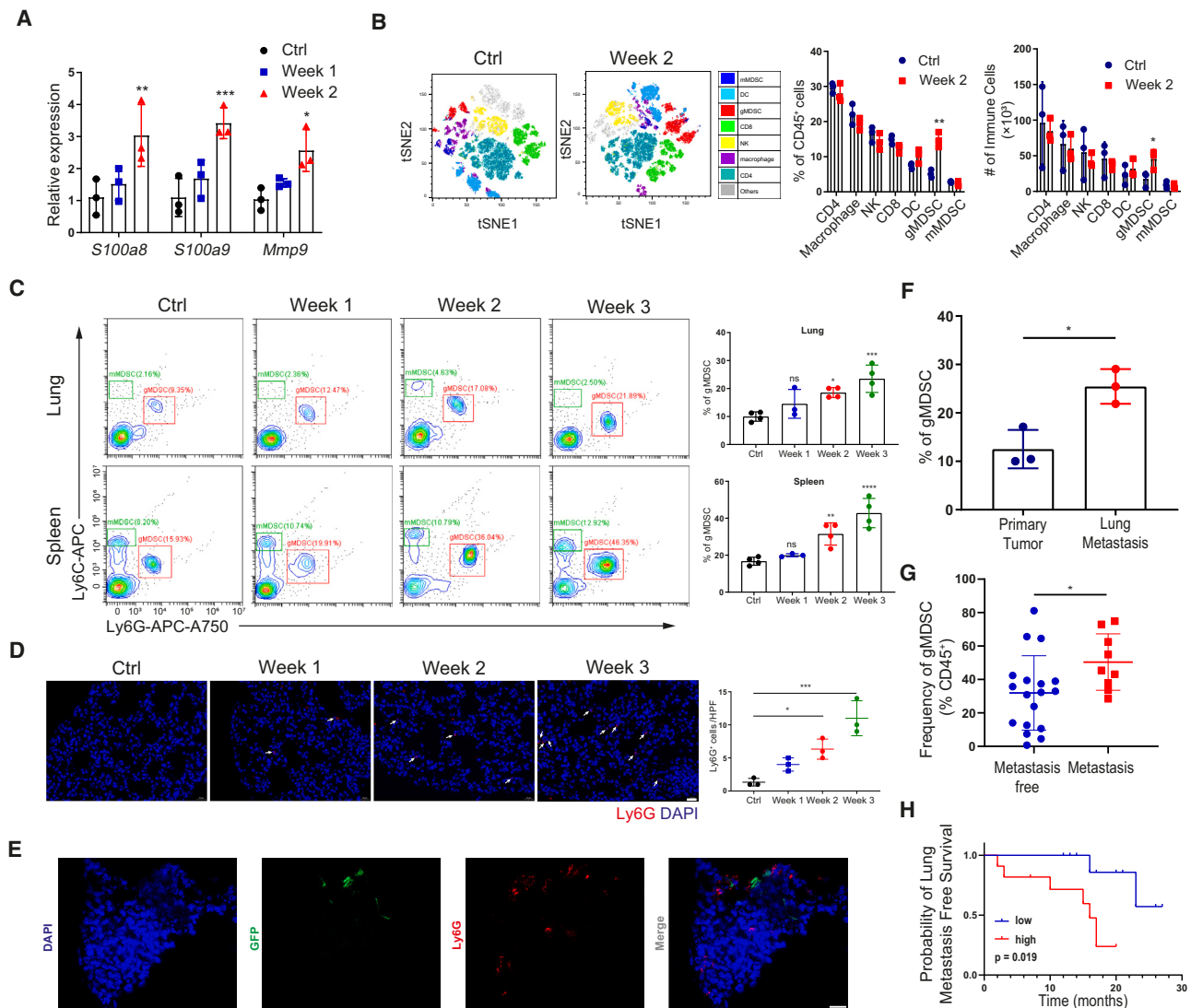
Figure 1. gMDSCs infiltrate the lung PMN of osteosarcoma and are associated with lung metastasis

(A) Pro-metastatic gene expression in the lungs 1 and 2 weeks after K7M2 tumor inoculation. The data were normalized to tumor-free mice. Gapdh was assayed as a control (n = 3 mice per group).

(B) Representative tSNE plots of infiltrating immune cells analyzed by FACS from the lungs of tumor-free and tumor-bearing mice at 2 weeks. Histograms show the quantification of fractions and overall numbers of infiltrating immune cell subsets (n = 3 mice per group).

(C) Representative FACS plots and quantification of the proportion of gMDSCs in the lungs and spleen detected by FACS in the mice 0–3 weeks after K7M2 tumor inoculation (n = 3 or 4).

(D) Representative images and quantification of Ly6G$^+$ cells in the lungs, detected by immunofluorescent staining (scale bar, 20 μm). Arrows indicate Ly6G$^+$ cells.

(E) GFP and Ly6G staining in mouse lungs 2 weeks after orthotopic implantation of K7M2-GFP cells (scale bar, 20 μm).

(F) Quantification of the proportion of gMDSCs in primary bone lesion and matched lung metastasis detected by FACS in the mice 3 weeks after K7M2 tumor inoculation (n = 3 mice per group).

(G) Peripheral gMDSC level in metastatic patients (who presented with or developed lung metastasis in 1 year; n = 9) and metastasis-free patients (n = 18), detected by FACS.

(H) Lung metastasis-free survival in osteosarcoma patients who presented without lung metastasis according to the level of peripheral gMDSCs (p = 0.019, Kaplan-Meier test). The median value was used as the cutoff point (high level, n = 10 patients; low level, n = 9 patients). Shown is one of the three independent experiments performed.

All data present mean ± SD, and p values were calculated by unpaired Student's t test in (B), (F), and (G) and by one-way ANOVA in (A), (C), and (D).

Rab27a also inhibited primary tumor growth (Figure S4F). Accordingly, the presence of Ly6G$^+$ gMDSCs in the lungs was remarkably diminished (Figure 3G). Overall, we demonstrated that tumor-cell-derived EVs mediated the accumulation of gMDSCs and the establishment of the lung PMN in osteosarcoma.
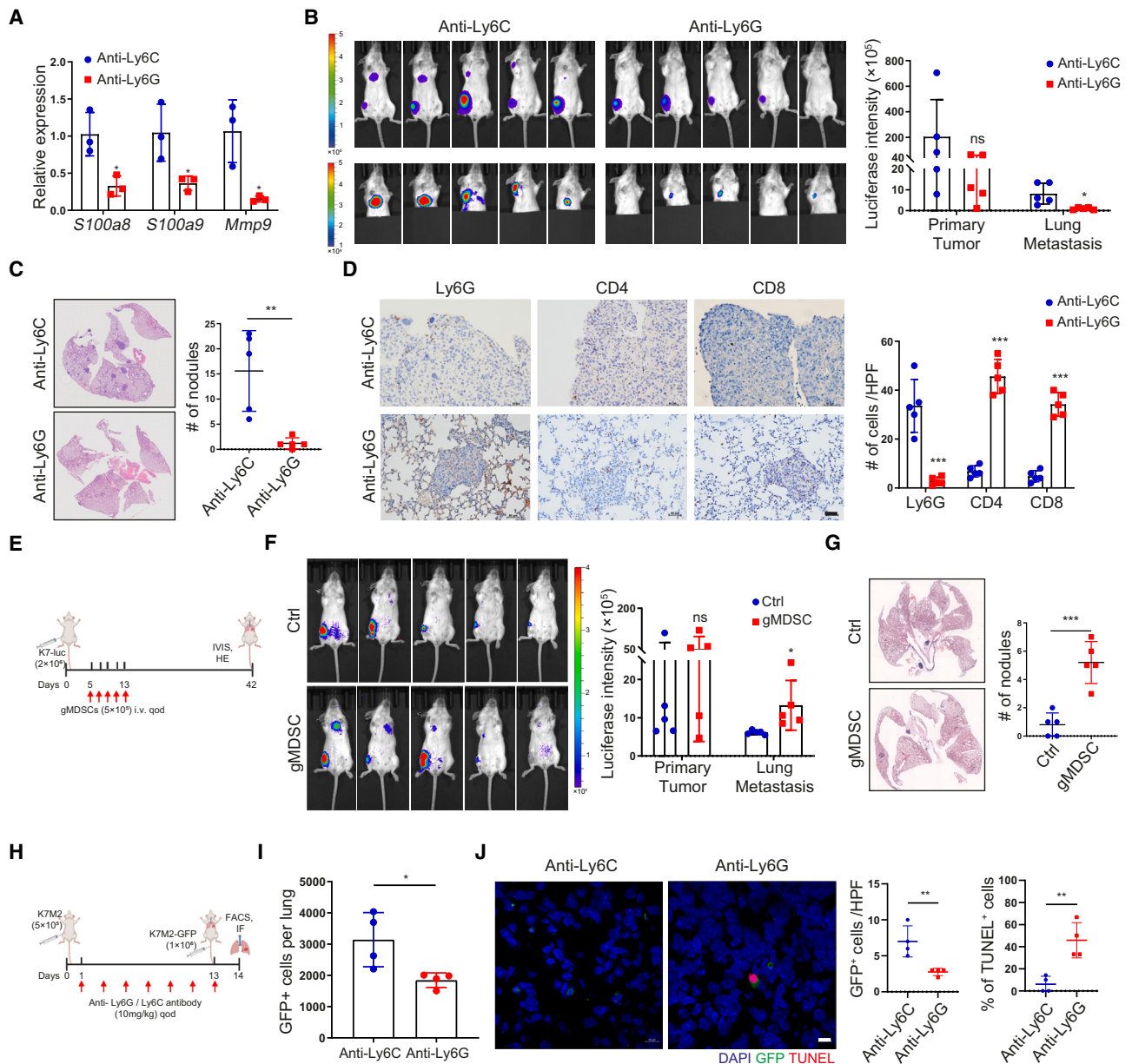
Figure 2. Infiltration of gMDSCs in the lung PMN facilitates tumor cell colonization and promotes lung metastasis

(A) RT-qPCR analyses of the indicated genes in the lungs of orthotopic K7M2-bearing mice treated with anti-Ly6G or anti-Ly6C antibody for 2 weeks. Gapdh was assayed as a control (n = 3 mice per group).

(B) Bioluminescence images and quantification of primary tumor (top) and lung metastasis (bottom) in mice treated with anti-Ly6G or anti-Ly6C antibody (n = 5).

(C) Representative H&E-stained lung sections and quantification of metastatic nodules in mice as described in (B).

(D) Representative immunohistochemistry (IHC) staining and quantification of Ly6G, CD4, and CD8 in lung sections from (B) (scale bar, 50 μm).

(E) The experimental procedure for adoptive transfer of gMDSCs or Gr1$^+$Ly6G$^-$ cells.

(F) Bioluminescence images and quantification of lung metastasis in mice treated as described in (E) (n = 5 mice per group).

(G) Representative H&E-stained lung sections and quantification of metastatic nodules in mice as described in (F).

(H) The experimental procedure for colonization of osteosarcoma cells in the lungs.

(I) Quantification of lung-colonized GFP-K7M2 cells detected by FACS in mice treated as described in (H) (n = 3 mice per group).

(J) TUNEL (red) combined with GFP (green) staining in mouse lungs treated as described in (H). The apoptosis rate of colonized tumor cells was calculated as double-positive cells in GFP$^+$ (K7M2) cells. White arrows indicate GFP$^+$ cells (n = 4 mice per group). Scale bar, 10 μm.

All data present mean ± SD, and p values were calculated by unpaired Student's t test.
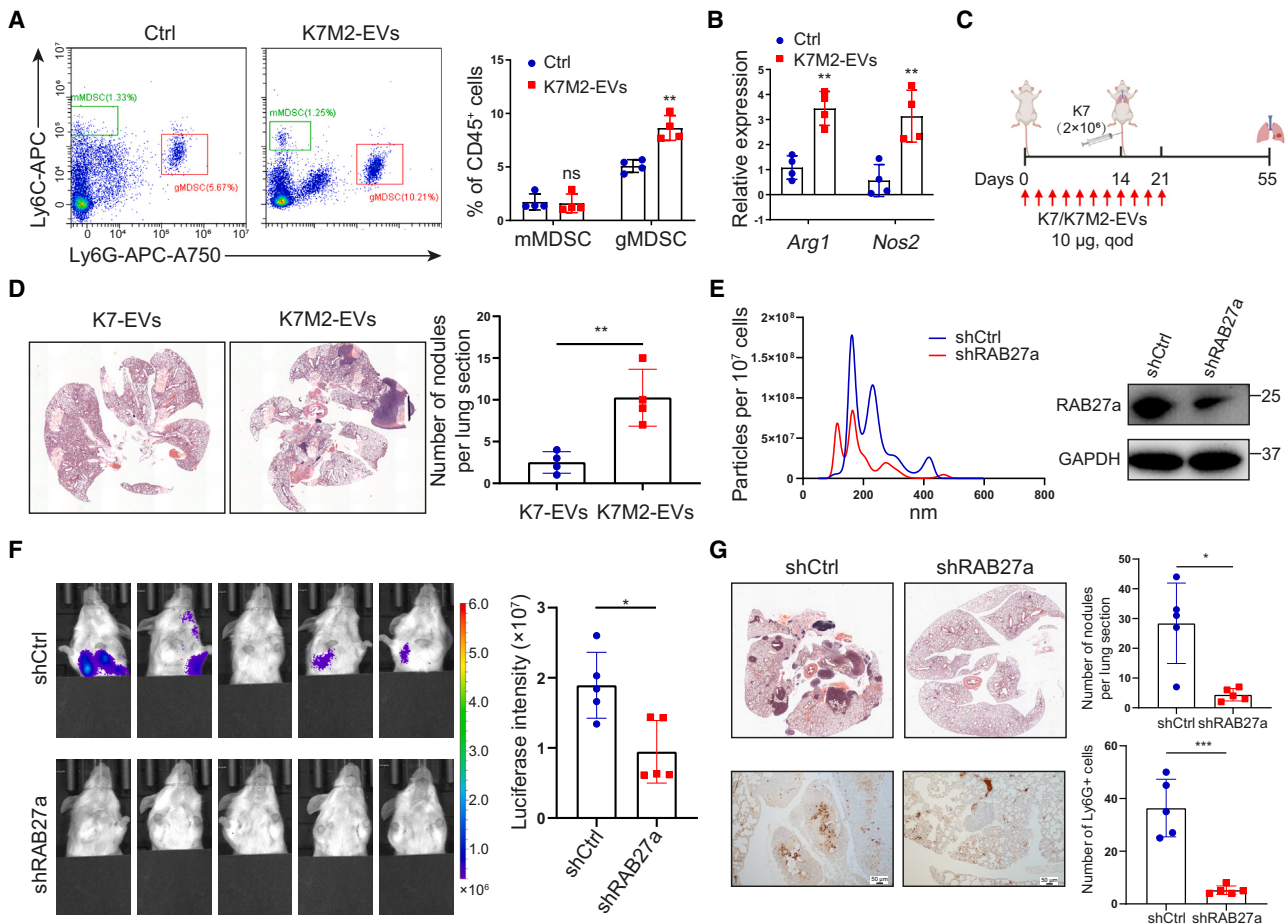
Figure 3. Osteosarcoma-cell-derived EVs promote lung metastasis by mediating the recruitment of gMDSCs

(A) Representative FACS plots and quantification of the proportion of mMDSCs and gMDSCs in the lungs of mice educated with K7M2-EVs for 2 weeks (n = 4 mice per group).

(B) RTqPCR analyses of the indicated genes in the lungs of mice treated as described in (A) (n = 4 mice per group).

(C) The experimental procedure for EV education.

(D) Representative H&E-stained lung sections and quantification of metastatic nodules in mice treated as described in (C).

(E) Histogram (left) showing the size distribution and particle concentration of EVs harvested from the same volume of supernatant of K7M2-shRAB27a and K7M2-shCtrl cells and western blot (WB) showing the knockdown efficacy of shRAB27a in K7M2 (right).

(F) Bioluminescence images and quantification of lung metastasis 4 weeks after orthotopic implantation of K7M2-shRAB27a and K7M2-shCtrl cells (n = 5 mice per group).

(G) Top: representative H&E-stained lung sections and quantification of metastatic nodules in mice as described in (F). Bottom: representative Ly6G staining and quantification of Ly6G$^+$ cells. Scale bar, 50 μm.

All data present mean ± SD, and p values were calculated by unpaired Student's t test.

Lung macrophages activated by osteosarcoma-cell-derived EVs recruit gMDSCs via CXCL2

To identify the recipient cells of osteosarcoma-derived EVs, we first evaluated the organic distribution of exogenously administered EVs. DiR-labeled EVs were enriched in the lungs 24 h after injection (Figure 4A). EVs could also be detected in the bone, liver, and spleen but not heart and muscle (Figure S4G). Moreover, fluorescence-activated cell sorting (FACS) results showed that EV$^+$ cells were mainly CD11b$^+$F4/80$^+$ macrophages (Figure 4B). Of note, EV$^+$ macrophages were mostly CD11c$^-$ Siglec-F$^-$CSF1R$^+$ lung interstitial macrophages (Figure 4C).[18] Meanwhile, uptake was not observed in epithelial or endothelial

cells (Figure S4H). Immunofluorescence (IF) staining of lung tissue sections confirmed the internalization of EVs by macrophages (Figure 4D). An *in vitro* uptake assay in sorted F4/80$^+$ and F4/80$^-$ cells from mouse lungs also verified the preferential uptake of EVs by macrophages (Figure 4E). Primary bone-marrow-derived macrophages (BMDMs) could take up EVs and exhibit dramatic changes in cell shape: more pseudopods (Figures 4E; S4I). In addition, depletion of macrophages with clodronate liposomes significantly abolished the pro-metastatic and Ly6G$^+$ gMDSC accumulation effect of K7M2-EVs (Figures 4F–4I).

To profile the molecular changes caused by osteosarcoma-cell-derived EVs, we performed RNA-seq of BMDMs treated
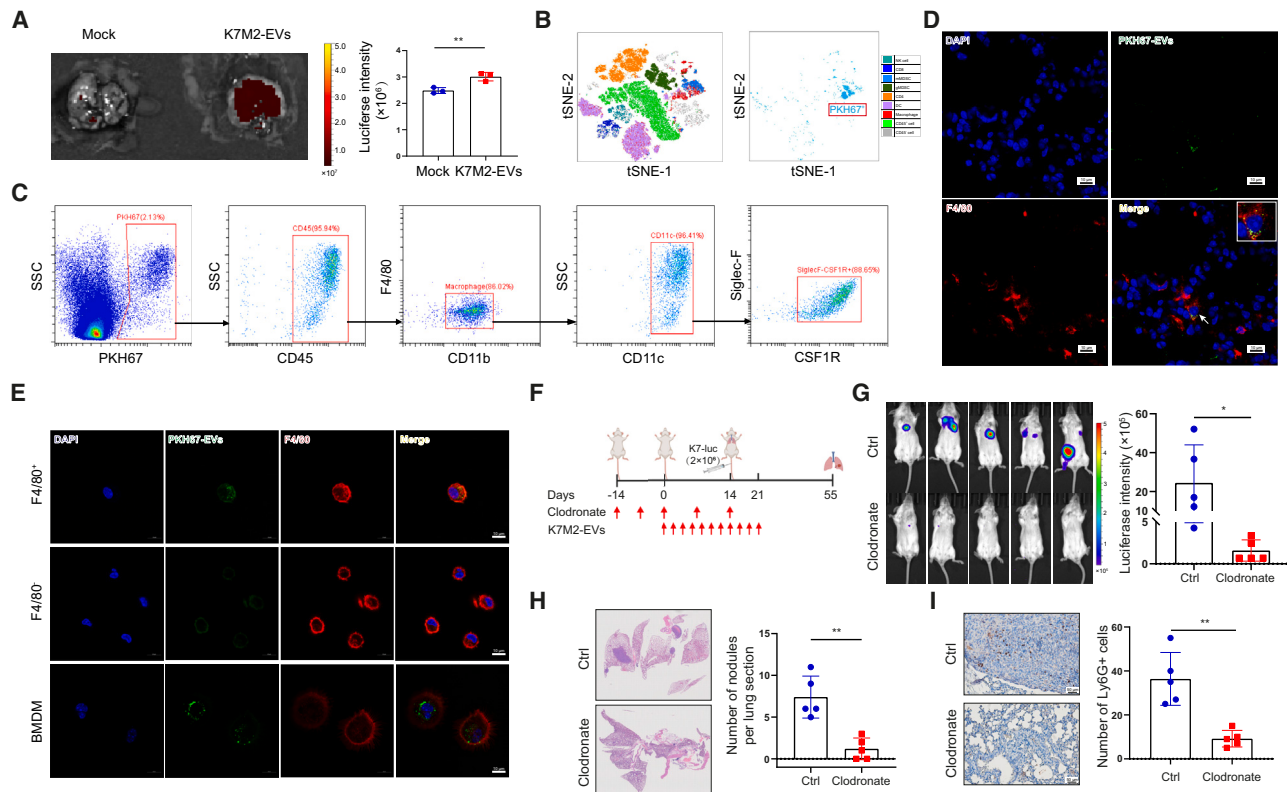
Figure 4. Osteosarcoma-cell-derived EVs target lung interstitial macrophages

(A) Representative images and quantification of dir-labeled K7M2-derived EVs or mock-prepared DiR dye control in the lungs by *ex vivo* bioluminescence imaging 24 h after intravenous injection (n = 3 mice per group).

(B) tSNE plots of infiltrating immune cells and PKH67-labeled K7M2-EVs analyzed by FACS 24 h after intravenous injection.

(C) PKH67-labeled K7M2-derived EV incorporation by CD45$^+$CD11b$^+$F4/80$^+$CD11c$^-$ lung interstitial macrophages was detected by flow cytometry.

(D) Representative IF images showing the colocalization (white arrow) of F4/80$^+$ macrophages and PKH67-labeled K7M2-derived EVs in mouse lungs treated as described in (B). The area marked by the white box is shown magnified in the inset at the top right. Scale bar, 10 μm.

(E) Normal mouse lung was harvested and sorted into F4/80$^+$ macrophages (top) and F4/80$^-$ cells (center) using anti-F4/80 MicroBeads. BMDMs (bottom) were cultured from normal mouse bone marrow. Representative IF images show the uptake of PKH67-labeled K7M2-derived EVs 24 h after EV treatment. Scale bar, 10 μm.

(F) The procedure for macrophage depletion in the EV education experiment.

(G) Bioluminescence images and quantification of lung metastasis 6 weeks after intravenous (i.v.) injection of K7-luc cells (n = 5 mice per group).

(H) Representative H&E-stained lung sections and quantification of metastatic nodules in mice from (G).

(I) Representative IHC staining and quantification of Ly6G in lung sections from (G).

Shown is one of the three independent experiments performed. All data present mean ± SD, and p values were calculated by unpaired Student's t test.

with EVs. GSE69607 and GSE32690 are gene expression datasets of BMDMs exhibiting polarization toward M1 and M2 and M2b, respectively. A heatmap and gene set enrichment analysis (GSEA) showed that EV-treated BMDMs presented mixed polarization toward the M1 and M2b phenotypes (Figures 5A and 5B). Accordingly, qPCR revealed a marked increase in the expression of *Il-6* and *Tnf-α* and a decrease in the expression of *Arg1* and *Cd206* when treated with K7M2-EVs (Figure 5C). An *in vitro* chemoattraction assay revealed that EV-induced activation of macrophages was responsible for the recruitment of gMDSCs (Figure 5D). Moreover, compared with that of BMDMs treated with either K7-EVs or interleukin-4 (IL-4), a prototypic cytokine used for *in vitro* polarization of "alternatively activated" M2 macrophages,[19] the supernatant of BMDMs treated with K7M2-EVs induced the most efficient chemotaxis in gMDSCs (Figure 5D).

The chemokine signaling pathway was enriched in osteosarcoma EV-treated BMDMs (Figure S4J). So, we next analyzed chemokines that were upregulated in BMDMs treated with K7M2-EVs based on the mRNA expression profile (Figure 5E). *Cxcl2* was one of the most upregulated chemokines, and this was further verified by qPCR (Figure 5F). In addition, the expression of *Cxcl2* was markedly elevated in the mouse lung PMN (Figure 5G). In accordance with the results of the *in vitro* chemoattraction assay, the greatest increase in CXCL2 secretion was observed in the supernatant of BMDMs treated with K7M2-EVs (Figure 5H). Neutralization of CXCL2 with a specific antibody markedly decreased the number of migrating gMDSCs in the chemotaxis assay (Figure 5I). In line with a previous report,[20] we showed that gMDSCs that infiltrated the mouse premetastatic lungs were positive for CXCR2, the G protein-coupled
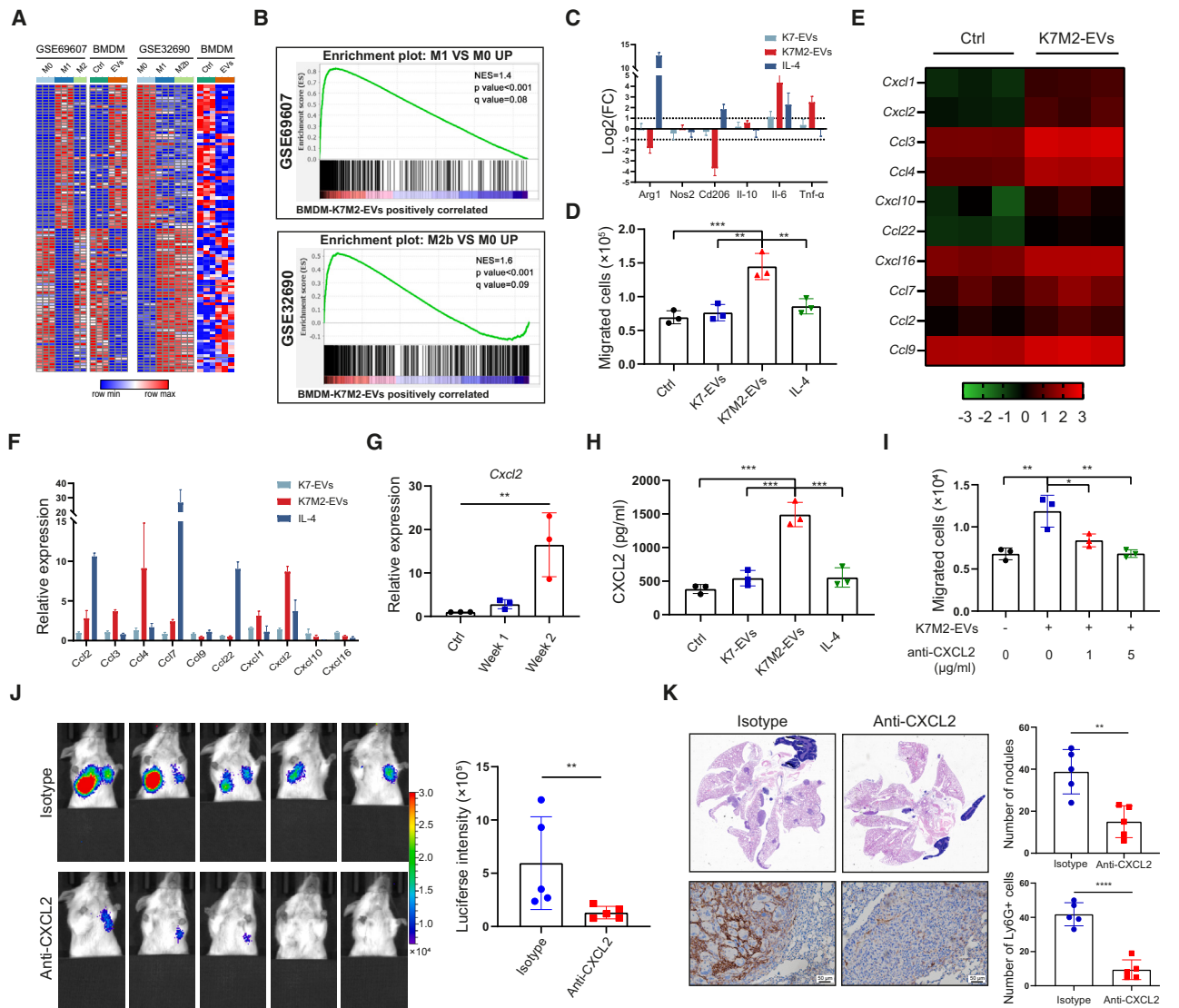
Figure 5. Osteosarcoma-cell-derived EVs induce CXCL2 secretion in macrophages to recruit gMDSCs

(A) Heatmaps showing the comparison of expression profiles between BMDMs treated with K7M2-EVs for 24 h and published RNA-seq data of M1, M2, and M2b polarized macrophages, extracted from GEO datasets GSE69607 (left) and GSE32690 (right).

(B) GSEA showing that the M1 and M2B gene signatures were enriched significantly in BMDMs treated with K7M2-EVs.

(C) RT-qPCR analyses of the common M1 and M2 macrophage marker genes in BMDMs treated with K7-EVs and K7M2-EVs. PBS and IL-4 were used as a negative and positive control, respectively. The data were normalized to the PBS group. Gapdh was assayed as a control.

(D) In vitro chemotaxis assay of gMDSCs from K7M2-bearing mouse lungs using conditioned medium of BMDMs treated with PBS, K7-EVs, K7M2-EVs, and IL-4.

(E) Heatmap showing the top 10 upregulated chemokines in K7M2-EV-treated BMDMs, based on the RNA-seq data in (A).

(F) RT-qPCR analyses of the top 10 upregulated chemokines in BMDMs treated with K7-EVs, K7M2-EVs, and IL-4 compared with PBS for 24 h.

(G) RT-qPCR analyses of Cxcl2 expression in premetastatic lungs 1 and 2 weeks after orthotopic K7M2 implantation (n = 3 mice per group). The data were normalized to the tumor-free group. Gapdh was assayed as a control.

(H) Quantification of CXCL2 in the supernatants of BMDMs treated with PBS, K7-EVs, K7M2-EVs, and IL-4 for 24 h.

(I) In vitro chemotaxis assay of gMDSCs using conditioned medium of BMDMs treated with K7M2-EVs (10 μg) with the indicated concentrations of anti-CXCL2 antibody or isotype control for 24 h.

(J) Bioluminescence images and quantification of lung metastasis in mice treated with the anti-CXCL2 antibody or isotype control (n = 5 mice per group).

(K) Top: representative H&E-stained lung sections and quantification of metastatic nodules in mice as described in (J). Bottom: representative Ly6G staining and quantification of Ly6G⁺ cells.

All data present mean ± SD, and p values were calculated by one-way ANOVA in (D) and (G)–(I) and unpaired Student's t test in (J) and (K).
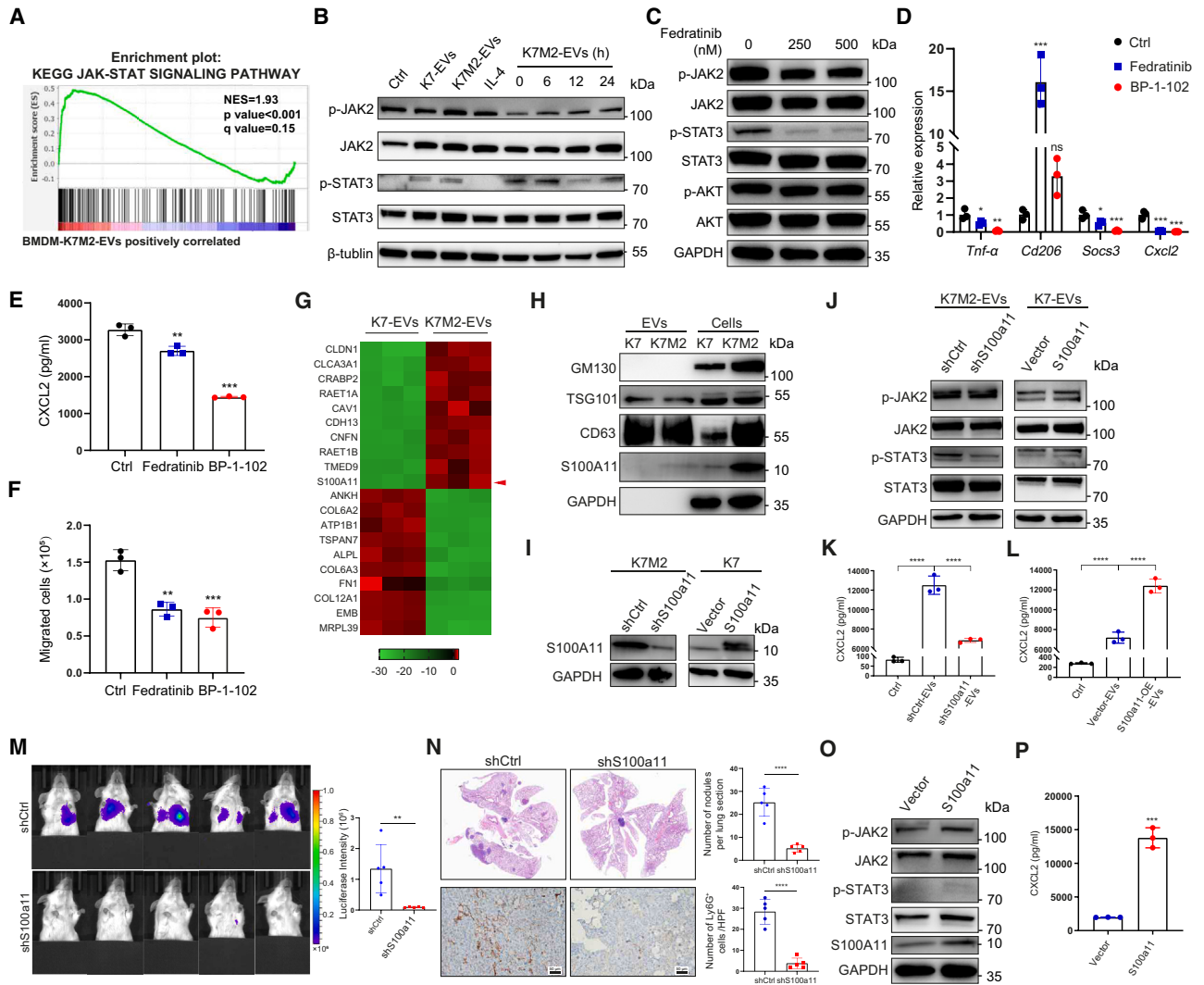
Figure 6. S100A11 transmitted by EVs activates JAK2-STAT3 signaling pathway in macrophages

(A) The JAK-STAT signaling pathway was significantly enriched in BMDMs treated with K7M2-EVs, as analyzed by GSEA.

(B) BMDMs were treated with PBS-ctrl, K7-EVs, K7M2-EVs, and IL-4 for 24 h or K7M2-EVs for the indicated times. Phosphorylation of JAK2 and STAT3 and their corresponding total levels were detected by immunoblot. Three independent experiments were performed.

(C) Phosphorylation of JAK2, STAT3, AKT, and their corresponding total levels in K7M2-EV-stimulated BMDMs with different concentrations of the JAK2 inhibitor fedratinib (0, 250, and 500 nM). Three independent experiments were performed.

(D) RT-qPCR analyses of the indicated genes in BMDMs treated with K7M2-Exo with fedratinib (250 nM) or BP-1-102 (1 μM) for 24 h (n = 3).

(E) Quantification of CXCL2 in the supernatants of BMDMs treated as described in (D).

(F) *In vitro* chemotaxis assay of gMDSCs using conditioned media from (D).

(G) Heatmaps showing the top 10 upregulated and downregulated protein cargos in K7M2-EVs compared with K7-EVs, as detected by liquid chromatography-MS (n = 3 per group). A red triangle marks the upregulated protein S100A11 in K7M2-EVs.

(H) Expression of S100A11 and the indicated EV markers in cell lines and their corresponding EVs detected by WB. GAPDH was used as a control for total cell lysate.

(I) WB showing the knockdown efficacy of shS100a11 in K7M2 cells and overexpression of S100A11 in K7 cells.

(J) Phosphorylation of JAK2 and STAT3 and their corresponding total levels in BMDMs treated with EVs from K7M2-shCtrl, K7M2-shS100a11, K7-vector, or K7-S100a11 cell lines for 24 h

(K) ELISA detection of CXCL2 in the supernatants of BMDMs treated as described in (D) (n = 3).

(L) ELISA detection of CXCL2 in the supernatants of BMDMs treated with PBS-ctrl and EVs from K7-vector or K7-S100a11 for 24 h (n = 3).

(M) Bioluminescence images and quantification of lung metastasis 4 weeks after orthotopic implantation of K7M2-shCtrl and K7M2-shS100a11 cells (n = 5 mice per group).

(legend continued on next page)

receptor for the chemokine CXCL2 (Figure S4K). Indeed, recombinant mouse CXCL2 recruited gMDSCs in a dose-dependent manner, while the CXCR2 inhibitor SB225002 attenuated the chemoattractive effect (Figure S4L). Moreover, anti-CXCL2 neutralizing antibody treatment reduced the number of lung metastases and alleviated the infiltration of gMDSCs in the lung microenvironment (Figures 5J and 5K). Meanwhile, no effect on the growth of primary tumors was observed (Figure S4M). Overall, we found that CXCL2 secreted by macrophages that were activated by osteosarcoma cell EVs was responsible for recruiting gMDSCs into the lung PMN and critical for promoting lung metastasis.

EV-packaged S100A11 activates the JAK2/STAT3 pathway in macrophages

We next sought to investigate the detailed mechanism of the activation of macrophages induced by osteosarcoma EVs. GSEA revealed that the JAK/STAT signaling pathway was enriched in osteosarcoma EV-treated BMDMs (Figure 6A). Accordingly, we found that K7M2-EVs could induce the phosphorylation of JAK2 and STAT3. In addition, such an effect was time dependent, with the highest in 6 h (Figure 6B). The activation could be abolished by fedratinib, a selective inhibitor of JAK2 (Figure 6C). Upregulation of *Cd206* expression and downregulation of *Tnf-α*, *Socs3* and *Cxcl2* expression were observed by treatment with fedratinib or BP-1-102, a selective inhibitor of STAT3 (Figure 6D). The results of ELISAs and chemoattraction assays also indicated that EV-mediated secretion of CXCL2 and recruitment of gMDSCs were blocked by inhibition of JAK2 or STAT3 phosphorylation (Figures 6E and 6F).

EVs have been shown to be highly enriched in proteins with various functions, including organotropic metastasis.[21] Thus, we performed quantitative mass spectrometry analysis of EVs from highly metastatic K7M2 cells and poorly metastatic parental K7 cells. The normalized and standardized data are shown in Table S1. Among the highly upregulated proteins in K7M2-EVs (Figure 6G), only cornifelin (CNFN) and s100 calcium binding protein a11 (S100A11) correlated with poorer prognosis in osteosarcoma patients based on the GSE21257 dataset (Figure S5A). Since CNFN is a structural component of epidermal corneocytes, we focused on the other protein, S100A11. As shown in Figure 6H, K7M2 had much higher expression of S100A11 in both the cellular and extracellular fractions. As expected, knocking down S100A11 in K7M2-EVs attenuated the activation of JAK2-STAT3 signaling pathway, while overexpression in K7-EVs enhanced the activation (Figures 6I and 6J). The stimulation of CXCL2 secretion was also significantly abolished when cells were treated with K7M2-shS100A11-EVs (Figure 6K). Instead, a gain-of-function study showed that overexpression of S100A11 in K7 cells greatly increased the secretion of CXCL2 by BMDMs (Figure 6L). While knocking down S100A11 did not affect the growth and invasion ability of K7M2 cells *in vitro*

(Figures S5B and S5C), the growth of primary tumors was inhibited *in vivo*, although this was not statistically significant (Figure S5D). In addition, lung metastasis was greatly inhibited by S100A11 knockdown (Figures 6M and 6N). In parallel, the infiltration of Ly6G+ gMDSCs was reduced (Figure 6N).

Furthermore, the ectopic overexpression of S100A11 in Raw264.7 cells significantly increased the phosphorylation levels of JAK2 and STAT3 and induced the secretion of CXCL2 (Figures 6O and 6P). These results suggested that EV-packaged S100A11 derived from osteosarcoma cells was responsible for macrophage activation via the JAK2/STAT3 pathway.

S100A11 interacts with USP9X

To explore the mechanism by which the S100A11 protein activates macrophages, we screened potential proteins that interacted with S100A11 using immunoprecipitation-mass spectrometry (IP-MS) analysis. IP was performed in HEK293T cells overexpressing a FLAG-tagged vector or S100A11 (Figure 7A). 141 proteins were identified as potential proteins specifically interacting with S100A11, excluding non-specifically binding proteins (Figures 7B; Table S2). After reviewing published literature regarding these proteins, USP9X, a deubiquitinase that can stabilize the activated phosphorylated JAK2 protein, came to our attention (Figure S5E). The interaction of S100A11 and USP9X was validated by coIP and western blot (Figures 7C and 7D). Furthermore, overexpression of S100A11 in Raw264.7 cells increased the expression of USP9X and the levels of phosphorylated JAK2 and STAT3 (Figure 7E). Meanwhile, both pharmacological inhibition and small interfering RNA (siRNA)-mediated knockdown of USP9X could reverse the effect of K7M2-EVs (Figure 7F). As expected, the secretion of CXCL2 was also greatly abolished by inhibition of USP9X (Figures 7G and 7H). Based on these data, we concluded that S100A11 interacts with USP9X to activate the JAK2/STAT3 pathway in macrophages.

To extend our findings to human osteosarcoma, we investigated the relationship between S100A11 expression in surgical specimens and clinical outcomes in a cohort of 50 treatment-naive osteosarcoma patients in our center (Table S3). Different intensities of S100A11 staining are shown in Figure S5F. The expression level of S100A11 was higher in osteosarcoma patients presented with lung metastasis (Figure 7I). Also, a high level of S100A11 was positively correlated with reduced lung metastasis-free survival and overall survival (Figures 7J and 7K). Multivariate analyses revealed that high S100A11 expression, together with Enneking stage, were independent predictors of a poor prognosis (Table S4). These clinical data suggest that increased S100A11 expression may predict the poor prognosis of osteosarcoma patients.

Thus, we show that the activation of lung macrophages by tumor-EV-derived S100A11 can initiate the recruitment of gMDSCs and the establishment of the lung PMN, further

---

(N) Top: representative H&E-stained lung sections and quantification of metastatic nodules in mice as described in (F). Bottom: representative Ly6G staining and quantification of Ly6G+ cells.

(O) Phosphorylation of JAK2 and STAT3 and their corresponding total levels in the control or S100A11-overexpressing Raw264.7 cell line.

(P) ELISA detection of CXCL2 in the supernatants of control or S100A11 overexpressing Raw264.7 cells (n = 3).

All data present mean ± SD, and p values were calculated by one-way ANOVA in (D)–(F), (K), and (L) and unpaired Student's t test in (M), (N), and (P).

facilitating osteosarcoma cell colonization and metastasis to the lungs.

DISCUSSION

Prior studies have noted the importance of the lung immune microenvironment in the progression of lung metastasis in osteosarcoma.[22,23] However, it is still not entirely clear how primary osteosarcoma cells orchestrate the lung PMN to foster tumor cell colonization. The present study was designed to investigate the crosstalk between osteosarcoma cells and the lung PMN.

In this study, we explored the lung metastasis process in a K7M2 orthotopic model in immune-competent mice. The lung premetastatic phase lasts for approximately 2 weeks after orthotopic implantation. Then, we delineated, for the first time, the composition and evolution of immune cell infiltration in the lung PMN using multiparameter flow cytometry analysis. The most obvious finding to emerge from the analysis is that the number of gMDSCs, a subtype of MDSCs, increased profoundly in the lung PMN. The infiltration of gMDSCs in the PMN is critical for the colonization of osteosarcoma cells and the formation of lung metastasis. We additionally demonstrated that osteosarcoma-cell-derived EVs are mediators that contribute to the establishment of the lung PMN. Education of mice with highly metastatic EVs can promote lung metastasis of poorly metastatic osteosarcoma cell lines. It is interesting to note that osteosarcoma-cell-derived EVs are mostly internalized by lung interstitial macrophages, one of the main two subtypes of macrophages in the lung. In turn, the activation of lung interstitial macrophages initiates an influx of gMDSCs to the lung via secretion of CXCL2, one of the known chemokines responsible for recruiting gMDSCs.[24] Furthermore, MS profiling of EVs revealed that S100A11 is enriched in highly metastatic osteosarcoma-cell-derived EVs. Indeed, EV-packaged S100A11 stimulates macrophages by activating the JAK2/STAT3 signaling pathway, which is correlated with CXCL2 secretion.

Evidence illustrating the critical role of the PMN in the development of lung metastasis in osteosarcoma has been steadily accumulating.[14,25,26] One recent study explored the PMN in a 143-B orthotopic implantation model in immune-compromised mice.[14] The Researchers in that study demonstrated that the lung premetastatic phase lasts for approximately 12 days, which is in line with our finding. However, more precise timing and examination of the PMN by means such as two-photon fluorescence *ex vivo* live imaging techniques are warranted in further research.[27] In addition, they observed an influx and mobilization of CD11b^{+} myeloid cells in the lung PMN. However, the specific subtype of myeloid cells has not been further characterized. Many studies have confirmed that bone-marrow-derived CD11b^{+} myeloid cells, including macrophages, MDSCs, and neutrophils, contribute to PMN preparation.[8,28,29] Our findings obtained in this study corroborate these earlier findings. Moreover, our results are believed to be more substantial, as we thoroughly screened the infiltrated immune cells in the lung PMN and characterized the role of immune-suppressive Ly6G^{+} gMDSCs in promoting metastasis. Meanwhile, we could not rule out the possibility that other cells or subtypes still played a role in this process. So, a more comprehensive approach, such as single-cell

RNA-seq of all cells in the lungs, would help us better understand the cellular and molecular events shaping PMN.[30] MDSCs are a group of heterogeneous immature myeloid cells widely known as immune-suppressive cells that can inhibit T cell and natural killer (NK) cell activity. Ample evidence has supported the multifunctional features of MDSCs in promoting tumor growth, preparing a prometastatic niche, and dampening the efficacy of immunotherapy.[31,32] Despite the large number of published reports on MDSCs, it remains a great challenge to dissect the specific contributions of different subpopulations, especially polymorphonuclear neutrophils and gMDSCs (also known as polymorphonuclear MDSCs), due to the lack of reliable markers. In our present study, we characterized the main two subtypes of MDSCs, gMDSCs and mMDSCs, based on the expression of Ly6G and Ly6C. However, we believe that gMDSCs in the lung PMN may contain three different subpopulations, as indicated in the tSNE analysis of the results from multiparameter flow cytometry (Figure 1B). In fact, a recent interesting work by Veglia et al.[33] characterized the heterogeneity of polymorphonuclear neutrophils in cancer. They described three distinct populations of polymorphonuclear neutrophils in tumor-bearing mice: classical polymorphonuclear neutrophils, polymorphonuclear MDSCs, and activated polymorphonuclear MDSCs with potent immune-suppressive activity. Whether such subpopulations of MDSCs exist in the lung PMN of osteosarcoma is worthy of further exploration. One limitation of our current study is the lack of distinction between gMDSCs and neutrophils due to their complex phenotypical and morphological similarities. Veglia et al.[33] identified classically activated neutrophils as CD11b^{+}CD15^{+}CD16^{+}CD66b^{high}Arg1^{+/−}STAT3^{−}S100A9^{+}LOX^{−} and gMDSC as CD11b^{high}CD15^{high}CD66b^{high}CD33^{high}Arg1^{high}S100A9^{high}Lox1^{high}. Referring to previous tumor microenvironment studies without the distinction between these subtype cells, we utilized an anti-Ly6G antibody for an *in vivo* loss-of-function study of gMDSCs.[34,35] Of note, utilizing a single-cell RNA-seq technique may further determine the exact prometastatic subtype of gMDSCs and provide an approach for precision targeted therapy to protect against lung metastasis.

Tumor-cell-derived EVs have been revealed to play an indispensable role in mediating the crosstalk between tumor cells and stromal cells in distant target organs. Education of target cells with EV-packaged cargos determines the organotropism of metastasis by establishing the PMN.[29,36,37] In line with other tumor models, we discovered that osteosarcoma-derived EVs are responsible for recruiting gMDSCs to the lung PMN and that blockade of EV secretion can prevent the development of lung metastasis. This finding is partially contrary to a previous study by Mazumdar et al.,[14] in which, although EV education induced myeloid cell infiltration in the lungs, no differences were observed in the metastatic burden in severe combined immunodeficiency (SCID) mice.[14] This inconsistency may be due to the different mouse models used in our study: immune-competent BALB/c mice. We show that gMDSCs are involved in constructing an immune-suppressive niche by inhibiting CD4^{+} and CD8^{+} T cells. Therefore, the immune escape potential and prometastatic effect of osteosarcoma-cell-derived EVs should be validated in an immunocompetent context. Despite such discrepancies, their results obtained in different mouse models with
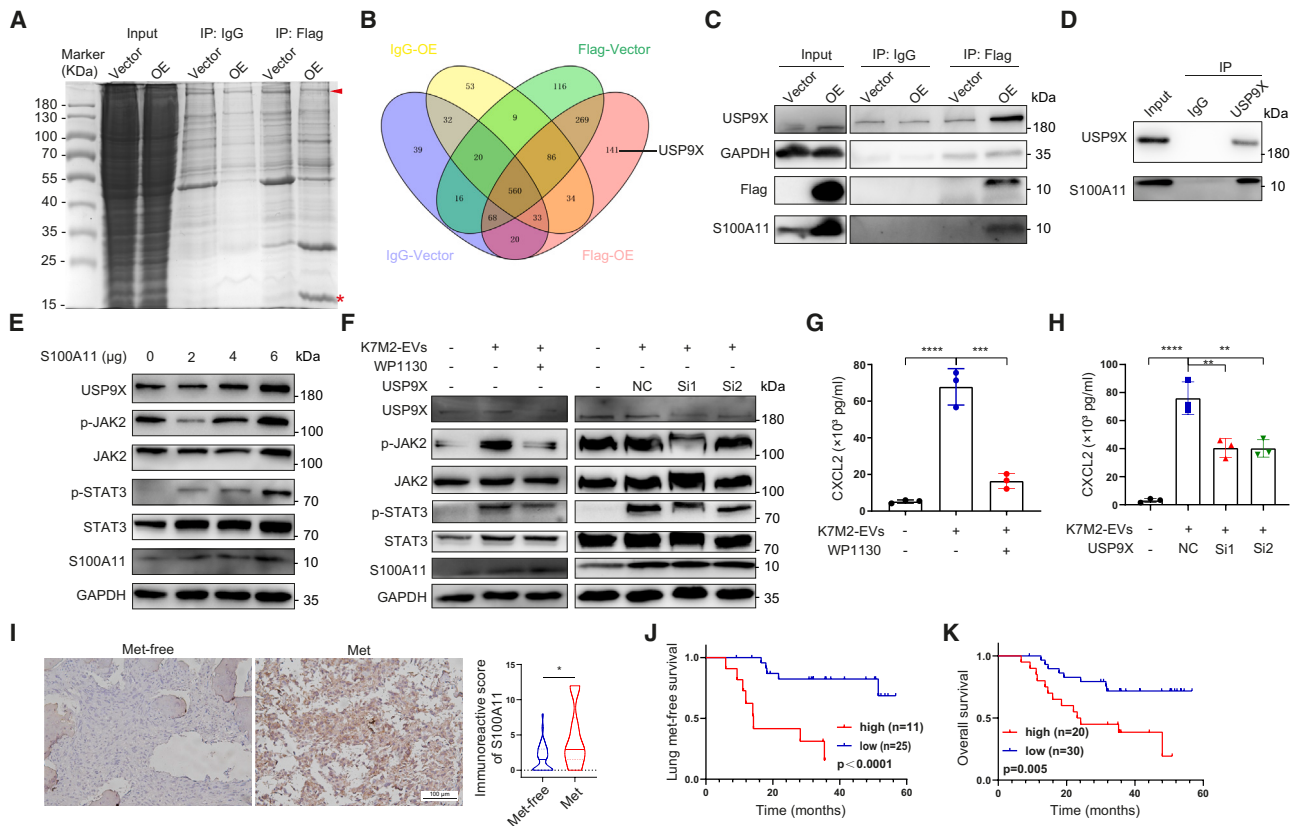
Figure 7. S100A11 executes its functions in macrophages by interacting with USP9X

(A) HEK293T cells were transfected with the indicated plasmids and then subjected to IP using anti-FLAG or immunoglobulin G (IgG) M2 beads. The samples were then subjected to SDS-PAGE followed by colloidal blue staining. A red triangle and asterisk mark the bands of USP9X and S100A11-FLAG, respectively.

(B) Venn diagram of S100A11-interacting proteins identified by IP-MS analysis. Detailed information about the 114 potential proteins specifically interacting with S100A11 are listed in Table S2.

(C) CoIP experiments were performed as described in (A), and the samples were analyzed by WB.

(D) The coIPs were performed in Raw264.7 cells with anti-IgG and anti-USP9X at their endogenous levels.

(E) Raw264.7 cells were transfected with the indicated amounts of plasmid expressing S100A11 for 48 h. Cell lysates were analyzed by WB.

(F) Raw264.7 cells were pre-treated with WP1130 (0.5 μM) for 24 h or siRNAs targeting USP9X for 48 h and then subjected to K7M2-EVs for another 24 h. Cell lysates were analyzed by WB.

(G and H) ELISA detection of CXCL2 in the supernatants of Raw264.7 cells treated as described in (E) (n = 3).

(I) Representative IHC staining images (left) of S100A11 in surgical specimens from osteosarcoma patients with (Met, n = 14) or without (Met free, n = 36) lung metastasis at presentation. Scale bars, 100 μm. Lines within the violin plot (right) mark the 25th, 50th, and 75th percentiles.

(J) Kaplan-Meier curves showing the lung metastasis-free survival of osteosarcoma patients without lung metastasis at presentation with high and low S100A11 expression.

(K) Kaplan-Meier curves showing the overall survival of osteosarcoma patients with high and low S100A11 expression.

The p values were calculated by one-way ANOVA in (G) and (H) and two-sided Mann-Whitney U test in (I). Survival analyses were performed using a two-sided log rank test.

human osteosarcoma cell lines corroborate our findings obtained in this study.

Osteosarcoma-cell-derived EVs have been proven to localize to the lungs in a previous report.[25] In another study, Rab22a-NeoF1 fusion protein-positive exosomes recruited BMDMs to facilitate pulmonary PMN formation in osteosarcoma.[26] Inspired by these previous studies, in the present study, we not only clarified the systemic distribution of osteosarcoma-derived EVs but also identified lung interstitial macrophages as the target cells in the lung. Although accumulating evidence shows that tumor-derived EVs determine the organotropism of metastasis,[21,37] we did not

observe an exclusive enrichment of osteosarcoma EVs in the mouse lung. Instead, osteosarcoma EVs localized to the lungs, bone, spleen, and liver after intravenous injection in mice, while the latter two organs may reflect the normal distribution of EVs as with ctrl dir liposomes (data not shown). We suppose that the accumulation of EVs in the bone tissue may be associated with the proliferation or invasion of primary tumor cells[38] or the establishment of a prometastatic niche for bone metastasis, which is the second most common site of metastasis in osteosarcoma.[39] In addition, inhibition of EV secretion could reduce primary tumor growth, which indicated that osteosarcoma EVs might also play a

role in the primary tumor microenvironment. Recently, a systematic review showed that the biodistribution of EVs was largely in the liver, lungs, kidneys, and spleen, regardless of the origin or size of EVs.[40] Hence, it is still unclear whether osteosarcoma-cell-derived EVs determine lung-specific metastatic tropism. It also remains to be further illustrated whether there are other target cells of osteosarcoma EVs in different organs.

There are two broad subtypes of macrophages in human and mouse lungs: alveolar macrophages, which exist in the alveolar cavity, and interstitial macrophages, which are localized in the interstitium.[41] Both subtypes of lung macrophages have been demonstrated to participate in the maintenance of lung homeostasis and regulation of the immune response.[42,43] Here, we showed that interstitial macrophages internalize EVs and then recruit gMDSCs. Indeed, it is rational to carry out the functional and mechanistic experiments with interstitial macrophages, which represents one limitation of our current study. According to the original mononuclear phagocyte system concept, circulating monocytes are the precursors for tissue macrophages.[44,45] In addition, both tissue-resident macrophages and bone-marrow-derived classical monocytes contribute to the accumulation of lung metastasis-associated macrophages.[46] So we utilized bone-marrow-derived cells as the *in vitro* model, which is broadly acceptable in various studies.[47,48] Tumor-associated macrophages (TAMs) play an important role in tumor development and metastasis and are marked by their plasticity and polarization.[49] Generally, TAMs can be classified into two main subtypes: classically activated antitumor (M1) and alternatively activated protumor (M2) macrophages. M2 TAMs can be further divided into M2a, M2b, M2c, and M2d subphenotypes. Indeed, previous studies have also demonstrated the prometastatic role of M2 TAMs in osteosarcoma.[26,50] Due to their substantial heterogeneity, an increasing number of researchers have pointed out that the polarization of TAMs should be regarded as a dynamic transition rather than a dichotomy, according to the stimuli in the tumor microenvironment.[51] Interestingly, we performed RNA-seq to profile the status of macrophages after stimulation with osteosarcoma EVs, which revealed a mixed polarization toward the M1 and M2b phenotypes. Therefore, we did not simply classify the activated macrophages as one specific subtype. Instead, we focused on the function of activated macrophages and identified the chemokine CXCL2, which recruits gMDSCs. However, we could not rule out other alterations of immune activities in activated macrophages, such as phagocytosis and antigen presentation. The important role of EV-activated lung macrophages in inducing immune suppression and tumor-promoting inflammation warrants further in-depth research. Notably, blockade of CXCL2 specifically attenuates lung metastasis *in vivo* and represents a potential therapeutic target for osteosarcoma.

At the molecular level, we found that S100A11 carried by osteosarcoma-cell-derived EVs activates macrophages via the JAK/STAT signaling pathway and further promotes lung PMN formation. S100A11 is a member of the S100 protein family and has been shown to be overexpressed in various cancer types.[52] Interestingly, a recent single-cell analysis study demonstrated that S100A11 was one of the top overexpressed genes in the lung metastatic lesions of osteosarcoma.[53] More-

over, S100A11 is also known as an inducer of certain inflammatory diseases, including rheumatoid arthritis and infective endocarditis.[54] This finding indicates that S100A11 may be involved in the regulation of certain immune processes. Indeed, research on parasite infection showed that, after infection by *Toxoplasma gondii*, S100A11 protein released from infected cells activates monocytes to secrete CCL2 as a form of protection against infection.[55] Here, we demonstrate that S100A11 is responsible for the activation of macrophages, mainly through the JAK/STAT pathway. Through IP-MS analysis, we identified that S100A11 could interacted with USP9X, a deubiquitinase shown previously to stabilize the activated phosphorylated JAK2.[56,57] Notably, pharmacological and genetic inhibition of USP9X could largely abolish the effect of S100A11-containing EVs on macrophages. We also found that overexpression of S100A11 could increase the protein level of USP9X in macrophages. However, the detailed mechanisms by which S100A11 stabilizes or enhances the activity of USP9X need to be further deciphered. In addition, a recent large-scale proteomics project confirmed that proteins in tumor-cell-derived EVs can serve as promising biomarkers for cancer detection.[11] Since S100A11 is enriched in highly metastatic osteosarcoma-cell-derived EVs, the predictive role of EV-S100A11 in lung metastasis of osteosarcoma needs to be validated in a large prospective patient cohort.

Limitations of the study

Here, we present that osteosarcoma-cell-derived EVs induced CXCL2 expression in lung interstitial macrophages, which mediated the recruitment of gMDSCs to the lung PMN. In accordance with published literature, the PMN is defined as a specialized microenvironment established before the formation of clinically detectable metastatic lesions in our present study. We defined week 1 to week 2 as the premetastatic phase of osteosarcoma, based on *in vivo* bioluminescence imaging, lung H&E staining, and RT-PCR of the luciferase gene. In fact, a similar time course (12 days) has been reported in another osteosarcoma-cell-line-derived xenograft model.[14] However, the data delineating this PMN were limited. There should be more comprehensive experiments, such as two-photon fluorescence *ex vivo* live imaging, to precisely demonstrate the dynamic evolution of the PMN in further research.[27]

In summary, our study not only dissected the composition of immune cells in the lung PMN but also illustrated the complex crosstalk mechanism between osteosarcoma cells and lung stromal cells mediated by EVs. These findings support the notion that circulating gMDSCs or EV-packaged S100A11 levels may be potential biomarkers for monitoring and indicating lung metastasis in osteosarcoma patients. Interrupting communication among primary tumor cells, macrophages, and gMDSCs is a promising therapeutic strategy for osteosarcoma lung metastasis.

STAR★METHODS

Detailed methods are provided in the online version of this paper and include the following:

Cell Reports
Article

SUPPLEMENTAL INFORMATION

Supplemental information can be found online at https://doi.org/10.1016/j.celrep.2024.113751.

AUTHOR CONTRIBUTIONS

J.W., Q.T., and C.D. designed the experiments. C.D., Y.X., H.C., X.Z., and Z.C. conducted the experiments. H.X., G.S., and J.L. provided samples from patients for clinical data analysis. C.D., L.H., and R.L. analyzed the data. C.D. and J.W. wrote the paper. J.W. and Q.T. are responsible for research supervision, coordination, and strategy.

DECLARATION OF INTERESTS

The authors declare no competing interests.

REFERENCES

1. Bielack, S.S., Kempf-Bielack, B., Delling, G., Exner, G.U., Flege, S., Helmke, K., Kotz, R., Salzer-Kuntschik, M., Werner, M., Winkelmann, W., et al. (2002). Prognostic factors in high-grade osteosarcoma of the extremities or trunk: an analysis of 1,702 patients treated on neoadjuvant cooperative osteosarcoma study group protocols. J. Clin. Oncol. *20*, 776–790. https://doi.org/10.1200/JCO.2002.20.3.776.

2. Smeland, S., Bielack, S.S., Whelan, J., Bernstein, M., Hogendoorn, P., Krailo, M.D., Gorlick, R., Janeway, K.A., Ingleby, F.C., Anninga, J., et al. (2019). Survival and prognosis with osteosarcoma: outcomes in more than 2000 patients in the EURAMOS-1 (European and American Osteosarcoma Study) cohort. Eur. J. Cancer *109*, 36–50. https://doi.org/10.1016/j.ejca.2018.11.027.

3. Mirabello, L., Troisi, R.J., and Savage, S.A. (2009). Osteosarcoma incidence and survival rates from 1973 to 2004: data from the Surveillance, Epidemiology, and End Results Program. Cancer *115*, 1531–1543. https://doi.org/10.1002/cncr.24121.

4. Psaila, B., and Lyden, D. (2009). The metastatic niche: adapting the foreign soil. Nat. Rev. Cancer *9*, 285–293. https://doi.org/10.1038/nrc2621.

5. Calon, A., Espinet, E., Palomo-Ponce, S., Tauriello, D.V.F., Iglesias, M., Céspedes, M.V., Sevillano, M., Nadal, C., Jung, P., Zhang, X.H.F., et al. (2012). Dependency of colorectal cancer on a TGF-β-driven program in stromal cells for metastasis initiation. Cancer Cell *22*, 571–584. https://doi.org/10.1016/j.ccr.2012.08.013.

6. Malanchi, I., Santamaria-Martínez, A., Susanto, E., Peng, H., Lehr, H.A., Delaloye, J.F., and Huelsken, J. (2011). Interactions between cancer stem cells and their niche govern metastatic colonization. Nature *481*, 85–89. https://doi.org/10.1038/nature10694.

7. Joyce, J.A., and Pollard, J.W. (2009). Microenvironmental regulation of metastasis. Nat. Rev. Cancer *9*, 239–252. https://doi.org/10.1038/nrc2618.

8. Kaplan, R.N., Riba, R.D., Zacharoulis, S., Bramley, A.H., Vincent, L., Costa, C., MacDonald, D.D., Jin, D.K., Shido, K., Kerns, S.A., et al. (2005). VEGFR1-positive haematopoietic bone marrow progenitors initiate the pre-metastatic niche. Nature *438*, 820–827. https://doi.org/10.1038/nature04186.

9. Wortzel, I., Dror, S., Kenific, C.M., and Lyden, D. (2019). Exosome-Mediated Metastasis: Communication from a Distance. Dev. Cell *49*, 347–360. https://doi.org/10.1016/j.devcel.2019.04.011.

10. Théry, C., Zitvogel, L., and Amigorena, S. (2002). Exosomes: composition, biogenesis and function. Nat. Rev. Immunol. *2*, 569–579. https://doi.org/10.1038/nri855.

11. Hoshino, A., Kim, H.S., Bojmar, L., Gyan, K.E., Cioffi, M., Hernandez, J., Zambirinis, C.P., Rodrigues, G., Molina, H., Heissel, S., et al. (2020). Extracellular Vesicle and Particle Biomarkers Define Multiple Human Cancers. Cell *182*, 1044–1061.e18. https://doi.org/10.1016/j.cell.2020.07.009.

12. García-Silva, S., Benito-Martín, A., Nogués, L., Hernández-Barranco, A., Mazariegos, M.S., Santos, V., Hergueta-Redondo, M., Ximénez-Embún, P., Kataru, R.P., Lopez, A.A., et al. (2021). Melanoma-derived small extracellular vesicles induce lymphangiogenesis and metastasis through an NGFR-dependent mechanism. Nat. Can. (Ott.) *2*, 1387–1405. https://doi.org/10.1038/s43018-021-00272-y.

13. Plebanek, M.P., Angeloni, N.L., Vinokour, E., Li, J., Henkin, A., Martinez-Marin, D., Filleur, S., Bhowmick, R., Henkin, J., Miller, S.D., et al. (2017). Pre-metastatic cancer exosomes induce immune surveillance by patrolling monocytes at the metastatic niche. Nat. Commun. *8*, 1319. https://doi.org/10.1038/s41467-017-01433-3.

14. Mazumdar, A., Urdinez, J., Boro, A., Arlt, M.J.E., Egli, F.E., Niederöst, B., Jaeger, P.K., Moschini, G., Muff, R., Fuchs, B., et al. (2020). Exploring the Role of Osteosarcoma-Derived Extracellular Vesicles in Pre-Metastatic Niche Formation and Metastasis in the 143-B Xenograft Mouse Osteosarcoma Model. Cancers *12*, 3457. https://doi.org/10.3390/cancers12113457.

15. Kumar, V., Patel, S., Tcyganov, E., and Gabrilovich, D.I. (2016). The Nature of Myeloid-Derived Suppressor Cells in the Tumor Microenvironment. Trends Immunol. *37*, 208–220. https://doi.org/10.1016/j.it.2016.01.004.

16. Celià-Terrassa, T., and Kang, Y. (2018). Metastatic niche functions and therapeutic opportunities. Nat. Cell Biol. *20*, 868–877. https://doi.org/10.1038/s41556-018-0145-9.

17. Peinado, H., Alečković, M., Lavotshkin, S., Matei, I., Costa-Silva, B., Moreno-Bueno, G., Hergueta-Redondo, M., Williams, C., García-Santos, G., Ghajar, C., et al. (2012). Melanoma exosomes educate bone marrow progenitor cells toward a pro-metastatic phenotype through MET. Nat. Med. *18*, 883–891. https://doi.org/10.1038/nm.2753.

18. Aegerter, H., Lambrecht, B.N., and Jakubzick, C.V. (2022). Biology of lung macrophages in health and disease. Immunity *55*, 1564–1580. https://doi.org/10.1016/j.immuni.2022.08.010.

19. Gordon, S., and Martinez, F.O. (2010). Alternative activation of macrophages: mechanism and functions. Immunity *32*, 593–604. https://doi.org/10.1016/j.immuni.2010.05.007.

20. Steele, C.W., Karim, S.A., Leach, J.D.G., Bailey, P., Upstill-Goddard, R., Rishi, L., Foth, M., Bryson, S., McDaid, K., Wilson, Z., et al. (2016). CXCR2 Inhibition Profoundly Suppresses Metastases and Augments Immunotherapy in Pancreatic Ductal Adenocarcinoma. Cancer Cell *29*, 832–845. https://doi.org/10.1016/j.ccell.2016.04.014.

21. Rodrigues, G., Hoshino, A., Kenific, C.M., Matei, I.R., Steiner, L., Freitas, D., Kim, H.S., Oxley, P.R., Scandariato, I., Casanova-Salas, I., et al. (2019). Tumour exosomal CEMIP protein promotes cancer cell colonization in brain metastasis. Nat. Cell Biol. *21*, 1403–1412. https://doi.org/10.1038/s41556-019-0404-4.

22. Namløs, H.M., Kresse, S.H., Müller, C.R., Henriksen, J., Holdhus, R., Sæter, G., Bruland, O.S., Bjerkehagen, B., Steen, V.M., and Myklebost, O. (2012). Global gene expression profiling of human osteosarcomas reveals metastasis-associated chemokine pattern. Sarcoma *2012*, 639038. https://doi.org/10.1155/2012/639038.

23. Ligon, J.A., Choi, W., Cojocaru, G., Fu, W., Hsiue, E.H.C., Oke, T.F., Siegel, N., Fong, M.H., Ladle, B., Pratilas, C.A., et al. (2021). Pathways of immune exclusion in metastatic osteosarcoma are associated with inferior patient outcomes. J. Immunother. Cancer *9*, e001772. https://doi.org/10.1136/jitc-2020-001772.

24. Taki, M., Abiko, K., Baba, T., Hamanishi, J., Yamaguchi, K., Murakami, R., Yamanoi, K., Horikawa, N., Hosoe, Y., Nakamura, E., et al. (2018). Snail promotes ovarian cancer progression by recruiting myeloid-derived suppressor cells via CXCR2 ligand upregulation. Nat. Commun. *9*, 1685. https://doi.org/10.1038/s41467-018-03966-7.

25. Charan, M., Dravid, P., Cam, M., Setty, B., Roberts, R.D., Houghton, P.J., and Cam, H. (2020). Tumor secreted ANGPTL2 facilitates recruitment of neutrophils to the lung to promote lung pre-metastatic niche formation and targeting ANGPTL2 signaling affects metastatic disease. Oncotarget *11*, 510–522. https://doi.org/10.18632/oncotarget.27433.

26. Zhong, L., Liao, D., Li, J., Liu, W., Wang, J., Zeng, C., Wang, X., Cao, Z., Zhang, R., Li, M., et al. (2021). Rab22a-NeoF1 fusion protein promotes osteosarcoma lung metastasis through its secretion into exosomes. Signal Transduct. Targeted Ther. *6*, 59. https://doi.org/10.1038/s41392-020-00414-1.

27. van den Bijgaart, R.J.E., Kong, N., Maynard, C., and Plaks, V. (2016). Ex vivo Live Imaging of Lung Metastasis and Their Microenvironment. J. Vis. Exp. e53741. https://doi.org/10.3791/53741.

28. Wculek, S.K., and Malanchi, I. (2015). Neutrophils support lung colonization of metastasis-initiating breast cancer cells. Nature *528*, 413–417. https://doi.org/10.1038/nature16140.

29. Liu, Y., Gu, Y., Han, Y., Zhang, Q., Jiang, Z., Zhang, X., Huang, B., Xu, X., Zheng, J., and Cao, X. (2016). Tumor Exosomal RNAs Promote Lung Pre-metastatic Niche Formation by Activating Alveolar Epithelial TLR3 to Recruit Neutrophils. Cancer Cell *30*, 243–256. https://doi.org/10.1016/j.ccell.2016.06.021.

30. Yofe, I., Shami, T., Cohen, N., Landsberger, T., Sheban, F., Stoler-Barak, L., Yalin, A., Phan, T.S., Li, B., Monteran, L., et al. (2023). Spatial and temporal mapping of breast cancer lung metastases identify TREM2 macrophages as regulators of the metastatic boundary. Cancer Discov. *13*, 2610–2631. https://doi.org/10.1158/2159-8290.Cd-23-0299.

31. Veglia, F., Sanseviero, E., and Gabrilovich, D.I. (2021). Myeloid-derived suppressor cells in the era of increasing myeloid cell diversity. Nat. Rev. Immunol. *21*, 485–498. https://doi.org/10.1038/s41577-020-00490-y.

32. Jayakumar, A., and Bothwell, A.L.M. (2019). Functional Diversity of Myeloid-Derived Suppressor Cells: The Multitasking Hydra of Cancer. J. Immunol. *203*, 1095–1103. https://doi.org/10.4049/jimmunol.1900500.

33. Veglia, F., Hashimoto, A., Dweep, H., Sanseviero, E., De Leo, A., Tcyganov, E., Kossenkov, A., Mulligan, C., Nam, B., Masters, G., et al. (2021). Analysis of classical neutrophils and polymorphonuclear myeloid-derived suppressor cells in cancer patients and tumor-bearing mice. J. Exp. Med. *218*, e20201803. https://doi.org/10.1084/jem.20201803.

34. Loeuillard, E., Yang, J., Buckarma, E., Wang, J., Liu, Y., Conboy, C., Pavelko, K.D., Li, Y., O'Brien, D., Wang, C., et al. (2020). Targeting tumor-associated macrophages and granulocytic-myeloid-derived suppressor cells augments pd-1 blockade in cholangiocarcinoma. J. Clin. Invest. *130*, 5380–5396. https://doi.org/10.1172/JCI137110.

35. Bayik, D., Zhou, Y., Park, C., Hong, C., Vail, D., Silver, D.J., Lauko, A., Roversi, G., Watson, D.C., Lo, A., et al. (2020). Myeloid-derived suppressor cell subsets drive glioblastoma growth in a sex-specific manner. Cancer Discov. *10*, 1210–1225. https://doi.org/10.1158/2159-8290.CD-19-1355.

36. Leary, N., Walser, S., He, Y., Cousin, N., Pereira, P., Gallo, A., Collado-Diaz, V., Halin, C., Garcia-Silva, S., Peinado, H., and Dieterich, L.C. (2022). Melanoma-derived extracellular vesicles mediate lymphatic remodelling and impair tumour immunity in draining lymph nodes. J. Extracell. Vesicles *11*, e12197. https://doi.org/10.1002/jev2.12197.

37. Hoshino, A., Costa-Silva, B., Shen, T.L., Rodrigues, G., Hashimoto, A., Tesic Mark, M., Molina, H., Kohsaka, S., Di Giannatale, A., Ceder, S., et al. (2015). Tumour exosome integrins determine organotropic metastasis. Nature *527*, 329–335. https://doi.org/10.1038/nature15756.

38. Perut, F., Roncuzzi, L., and Baldini, N. (2019). The Emerging Roles of Extracellular Vesicles in Osteosarcoma. Front. Oncol. *9*, 1342. https://doi.org/10.3389/fonc.2019.01342.

39. Lavit, E., Aldea, M., Piperno-Neumann, S., Firmin, N., Italiano, A., Isambert, N., Kurtz, J.E., Delcambre, C., Lebrun, V., Soibinet-Oudot, P., et al. (2022). Treatment of 120 adult osteosarcoma patients with metachronous and synchronous metastases: A retrospective series of the French Sarcoma Group. Int. J. Cancer *150*, 645–653. https://doi.org/10.1002/ijc.33823.

40. Kang, M., Jordan, V., Blenkiron, C., and Chamley, L.W. (2021). Biodistribution of extracellular vesicles following administration into animals: A systematic review. J. Extracell. Vesicles *10*, e12085. https://doi.org/10.1002/jev2.12085.

41. Hou, F., Xiao, K., Tang, L., and Xie, L. (2021). Diversity of Macrophages in Lung Homeostasis and Diseases. Front. Immunol. *12*, 753940. https://doi.org/10.3389/fimmu.2021.753940.

42. Arif, A.A., Huang, Y.H., Freeman, S.A., Atif, J., Dean, P., Lai, J.C.Y., Blanchet, M.R., Wiegand, K.C., McNagny, K.M., Underhill, T.M., et al. (2021). Inflammation-Induced Metastatic Colonization of the Lung Is Facilitated by Hepatocyte Growth Factor-Secreting Monocyte-Derived Macrophages. Mol. Cancer Res. *19*, 2096–2109. https://doi.org/10.1158/1541-7786.MCR-21-0009.

43. Keerthivasan, S., Şenbabaoğlu, Y., Martinez-Martin, N., Husain, B., Verschueren, E., Wong, A., Yang, Y.A., Sun, Y., Pham, V., Hinkle, T., et al. (2021). Homeostatic functions of monocytes and interstitial lung

macrophages are regulated via collagen domain-binding receptor LAIR1. Immunity *54*, 1511–1526.e8. https://doi.org/10.1016/j.immuni.2021.06.012.

44. Volkman, A., Chang, N.C., Strausbauch, P.H., and Morahan, P.S. (1983). Differential effects of chronic monocyte depletion on macrophage populations. Lab. Invest. *49*, 291–298.

45. Vanneste, D., Bai, Q., Hasan, S., Peng, W., Pirottin, D., Schyns, J., Maréchal, P., Ruscitti, C., Meunier, M., Liu, Z., et al. (2023). MafB-restricted local monocyte proliferation precedes lung interstitial macrophage differentiation. Nat. Immunol. *24*, 827–840. https://doi.org/10.1038/s41590-023-01468-3.

46. Loyher, P.L., Hamon, P., Laviron, M., Meghraoui-Kheddar, A., Goncalves, E., Deng, Z., Torstensson, S., Bercovici, N., Baudesson de Chanville, C., Combadière, B., et al. (2018). Macrophages of distinct origins contribute to tumor development in the lung. J. Exp. Med. *215*, 2536–2553. https://doi.org/10.1084/jem.20180534.

47. You, Y., Yuan, H., Min, H., Li, C., and Chen, J. (2023). Fibroblast-derived CXCL14 aggravates crystalline silica-induced pulmonary fibrosis by mediating polarization and recruitment of interstitial macrophages. J. Hazard Mater. *460*, 132489. https://doi.org/10.1016/j.jhazmat.2023.132489.

48. Wu, C., Zhong, Q., Shrestha, R., Wang, J., Hu, X., Li, H., Rouchka, E.C., Yan, J., and Ding, C. (2023). Reactive myelopoiesis and FX-expressing macrophages triggered by chemotherapy promote cancer lung metastasis. JCI Insight *8*, e167499. https://doi.org/10.1172/jci.insight.167499.

49. Noy, R., and Pollard, J.W. (2014). Tumor-associated macrophages: from mechanisms to therapy. Immunity *41*, 49–61. https://doi.org/10.1016/j.immuni.2014.06.010.

50. Wolf-Dennen, K., Gordon, N., and Kleinerman, E.S. (2020). Exosomal communication by metastatic osteosarcoma cells modulates alveolar macrophages to an M2 tumor-promoting phenotype and inhibits tumoricidal functions. OncoImmunology *9*, 1747677. https://doi.org/10.1080/2162402X.2020.1747677.

51. Martinez, F.O., and Gordon, S. (2014). The M1 and M2 paradigm of macrophage activation: time for reassessment. F1000Prime Rep. *6*, 13. https://doi.org/10.12703/P6-13.

52. Cross, S.S., Hamdy, F.C., Deloulme, J.C., and Rehman, I. (2005). Expression of S100 proteins in normal human tissues and common cancers using tissue microarrays: S100A6, S100A8, S100A9 and S100A11 are all overexpressed in common cancers. Histopathology *46*, 256–269. https://doi.org/10.1111/j.1365-2559.2005.02097.x.

53. Zhou, Y., Yang, D., Yang, Q., Lv, X., Huang, W., Zhou, Z., Wang, Y., Zhang, Z., Yuan, T., Ding, X., et al. (2020). Single-cell RNA landscape of intratumoral heterogeneity and immunosuppressive microenvironment in advanced osteosarcoma. Nat. Commun. *11*, 6322. https://doi.org/10.1038/s41467-020-20059-6.

54. Zhang, L., Zhu, T., Miao, H., and Liang, B. (2021). The Calcium Binding Protein S100A11 and Its Roles in Diseases. Front. Cell Dev. Biol. *9*, 693262. https://doi.org/10.3389/fcell.2021.693262.

55. Safronova, A., Araujo, A., Camanzo, E.T., Moon, T.J., Elliott, M.R., Beiting, D.P., and Yarovinsky, F. (2019). Alarmin S100A11 initiates a chemokine response to the human pathogen Toxoplasma gondii. Nat. Immunol. *20*, 64–72. https://doi.org/10.1038/s41590-018-0250-8.

56. Naik, E., and Dixit, V.M. (2016). Usp9X Is Required for Lymphocyte Activation and Homeostasis through Its Control of ZAP70 Ubiquitination and PKCbeta Kinase Activity. J. Immunol. *196*, 3438–3451. https://doi.org/10.4049/jimmunol.1403165.

57. Schwartzman, O., Savino, A.M., Gombert, M., Palmi, C., Cario, G., Schrappe, M., Eckert, C., von Stackelberg, A., Huang, J.Y., Hameiri-Grossman, M., et al. (2017). Suppressors and activators of JAK-STAT signaling at diagnosis and relapse of acute lymphoblastic leukemia in Down syndrome. Proc. Natl. Acad. Sci. USA *114*, E4030–E4039. https://doi.org/10.1073/pnas.1702489114.

58. Love, M.I., Huber, W., and Anders, S. (2014). Moderated estimation of fold change and dispersion for RNA-seq data with DESeq2. Genome Biol. *15*, 550. https://doi.org/10.1186/s13059-014-0550-8.

59. Yu, G., Wang, L.G., Han, Y., and He, Q.Y. (2012). clusterProfiler: an R package for comparing biological themes among gene clusters. OMICS *16*, 284–287. https://doi.org/10.1089/omi.2011.0118.

60. Théry, C., Amigorena, S., Raposo, G., and Clayton, A. (2006). Isolation and characterization of exosomes from cell culture supernatants and biological fluids. Curr. Protoc. Cell Biol. *30*. https://doi.org/10.1002/0471143030.cb0322s30.

61. Lu, J., Song, G., Tang, Q., Zou, C., Han, F., Zhao, Z., Yong, B., Yin, J., Xu, H., Xie, X., et al. (2015). IRX1 hypomethylation promotes osteosarcoma metastasis via induction of CXCL14/NF-kappaB signaling. J. Clin. Invest. *125*, 1839–1856. https://doi.org/10.1172/JCI78437.

62. Chen, F., Chen, J., Yang, L., Liu, J., Zhang, X., Zhang, Y., Tu, Q., Yin, D., Lin, D., Wong, P.P., et al. (2019). Extracellular vesicle-packaged HIF-1alpha-stabilizing lncRNA from tumour-associated macrophages regulates aerobic glycolysis of breast cancer cells. Nat. Cell Biol. *21*, 498–510. https://doi.org/10.1038/s41556-019-0299-0.

63. Meng, D.F., Sun, R., Liu, G.Y., Peng, L.X., Zheng, L.S., Xie, P., Lin, S.T., Mei, Y., Qiang, Y.Y., Li, C.Z., et al. (2020). S100A14 suppresses metastasis of nasopharyngeal carcinoma by inhibition of NF-kB signaling through degradation of IRAK1. Oncogene *39*, 5307–5322. https://doi.org/10.1038/s41388-020-1363-8.

STAR★METHODS

KEY RESOURCES TABLE

REAGENT or RESOURCE	SOURCE	IDENTIFIER
Antibodies		
InVivoMab anti-mouse Ly6G	BioXcell	Cat#BE0075; RRID: AB_1107721
InVivoMAb rat IgG2 isotype control	BioXcell	Cat#BE0089; RRID: AB_1107769
Anti-mouse CXCL2 (Clone 40605)	Leinco Technologies	Cat#M1277; RRID: AB_2831271
Rat IgG2b Isotype Control	Leinco Technologies	Cat#I-1034; RRID: AB_2737522
Rabbit monoclonal anti-JAK2(phospho Y1007 + Y1008)	Abcam	Cat#ab32101; RRID: AB_775808
Rabbit monoclonal anti-JAK2	Abcam	Cat#ab108596; RRID: AB_10865183
Rabbit monoclonal anti-CD63	Abcam	Cat#ab217345; RRID: AB_2754982
Rabbit monoclonal anti-GM130	Abcam	Cat#ab52649; RRID: AB_880266
Rabbit monoclonal anti-TSG101	Abcam	Cat#ab125011; RRID: AB_10974262
Rat monoclonal anti-Ly6G	Abcam	Cat#ab25377; RRID: AB_470492
Mosue monoclonal anti-P-Stat3(Y705)(M9C6)	Cell Signaling Technology	Cat#4113S; RRID: AB_2198588
Mosue monoclonal anti-STAT3	Cell Signaling Technology	Cat#9139S; RRID: AB_331757
Rabbit monoclonal anti-P-Stat1(Y701)(58D6)	Cell Signaling Technology	Cat#9167S; RRID: AB_561284
Rabbit monoclonal anti-STAT1	Cell Signaling Technology	Cat#9172S; RRID: AB_2198300
Rabbit monoclonal anti-P-Akt(S473)	Cell Signaling Technology	Cat#4060S; RRID: AB_2315049
Rabbit monoclonal anti-Akt(pan)	Cell Signaling Technology	Cat#4691S; RRID: AB_915783
Rabbit monoclonal anti-GAPDH(D16H11)	Cell Signaling Technology	Cat#5174S; RRID: AB_10622025
Rabbit monoclonal anti-USP9X	Cell Signaling Technology	Cat#14898S; RRID: AB_2798640
Rabbit monoclonal anti-F4/80	Cell Signaling Technology	Cat#30325T; RRID: AB_2798990
Rabbit polyclonal anti-Rab27a	Proteintech	Cat#17817-AP; RRID: AB_2176728
Mosue monoclonal anti-s100a11	Proteintech	Cat#60024-1-ig; RRID: AB_2238821
PE-CF594 anti-mouse CD45	BD biosciences	Cat#562420; RRID: AB_11154401
FVS510 anti-mouse Live/Dead	BD biosciences	Cat#564406; RRID: AB_2869572
FVS700 anti-mouse Live/Dead	BD biosciences	Cat# 564997; RRID: AB_2869637
FITC anti-mouse CD11B	BD biosciences	Cat#553310; RRID: AB_394774
APC-CY7 anti-mouse LY6G	BD biosciences	Cat#560599; RRID: AB_1727560
BV605 anti-mouse LY6C	BD biosciences	Cat#563011; RRID: AB_2737949
PE anti-mouse CD3	BD biosciences	Cat#553063; RRID: AB_394596
BV650 anti-mouse CD4	BD biosciences	Cat#563747; RRID: AB_2716859
AF700 anti-mouse CD8	BD biosciences	Cat#557959; RRID: AB_396959
BV421 anti-mouse F4/80	BD biosciences	Cat#565411; RRID: AB_2734779
AF647 anti-mouse CD206	BD biosciences	Cat#565250; RRID: AB_2739133
PE-CY7 anti-mouse CD11C	BD biosciences	Cat#558079; RRID: AB_647251
BV786 anti-mouse Siglec-F	BD biosciences	Cat# 740956; RRID: AB_2740581
BV605 anti-mouse CSF1R	BD biosciences	Cat# 743640; RRID: AB_2741650
BB700 anti-mouse CD31	BD biosciences	Cat# 742123; RRID: AB_2871389
Purified rat anti-mouse CD16/CD32	BD biosciences	Cat#553141; RRID: AB_394656
APC-Cy7 anti-human CD45	BD biosciences	Cat#557833; RRID: AB_396891
PE-Cy7 anti-human CD11b	BD biosciences	Cat#557743; RRID: AB_396849
APC anti-human HLA-DR	BD biosciences	Cat#559866; RRID: AB_398674
BV421 anti-human CD14	BD biosciences	Cat#563743; RRID: AB_2744289

Continued

REAGENT or RESOURCE	SOURCE	IDENTIFIER
FTIC anti-human CD15	BD biosciences	Cat#555401; RRID: AB_395801
PE anti-mouse Epcam	Biolegend	Cat# 118206; RRID: AB_1134172
PerCP-Cy5.5 anti-mouse CD49B	Biolegend	Cat#103519; RRID: AB_2566104
PE anti-mouse CXCR2	Biolegend	Cat#149303; RRID: AB_2565691
Rabbit polyclonal anti-human S100A11	Sino Biological	Cat#11140-T25
Rabbit polyclonal anti-mouse S100a11	Sino Biological	Cat#50227-T48
Anti-mouse CD4 antibody	Servicebio	GB11064; RRID: AB_2904187
Anti-mouse CD8 antibody	Servicebio	GB114196; RRID: AB_3064847
Anti-mouse CD3 antibody	Bio-Gems	Cat#05112-25
Anti-mouse CD28 antibody	Bio-Gems	Cat#10312-25;
Bacterial and virus strains		
One Shot™ Stbl3™ Chemically Competent E. coli	Thermo Fisher Scientific	Cat#C737303
Biological samples		
Tissue samples of osteosarcoma patients	Sun Yat-sen University Cancer Center	Sun Yat-sen University Cancer Center
Blood samples of osteosarcoma patients	Sun Yat-sen University Cancer Center	Sun Yat-sen University Cancer Center
Chemicals, peptides, and recombinant proteins		
Lipofectamine RNAiMAX Transfection Reagent	Thermo Fisher Scientific	Cat#13778150
Lipofectamine™ 3000 Transfection Reagent	Thermo Fisher Scientific	Cat#L3000015
ProLong Diamond Antifade Mountant with DAPI	Thermo Fisher Scientific	Cat#P36962
Recombinant murine M-CSF	PeproTech	Cat#315-02
Recombinant murine IL-2	PeproTech	Cat#212-12
Collagen I	Sigma-Aldrich	Cat#SCR103
Collagen IV	Sigma-Aldrich	Cat#C5138
Matrigel	Corning	Cat#354230
Clodronate liposomes	YEASEN	Cat#40337ES08
Control liposomes	YEASEN	Cat#40338ES05
D-Luciferin,Sodium Salt	YEASEN	Cat#40901ES03
TRITC Phalloidin	YEASEN	Cat#40734ES75
Puromycin	Takara Bio	Cat# 631306
DAPI	Sigma-Aldrich	Cat# D9542
Biotin	Sigma-Aldrich	Cat#B4501
Protease inhibitor cocktail	Selleck	Cat#B14001
Phosphatase Inhibitor Cocktail	Selleck	Cat#B15001
Clarity Western ECL Substrate	Bio-Rad	Cat#1705061
BD Horizon™ Brilliant Stain Buffer	BD Biosciences	Cat#566349
XenoLight DiR	PerkinElmer	Cat#125964
RBC Lysis Buffer	Biolegend	Cat#420301
Coomassie Blue Fast Staining Solution	Beyotime	Cat#P0017
Critical commercial assays		
Fixation/Permeablization Kit	BD Biosciences	Cat#554714
Transcription Factor Staining kit	eBioscience	Cat#00-5523-00
Pierce BCA Protein Assay Kit	Thermo Fisher Scientific	Cat#23225
cDNA synthesis kit	Vazyme	Cat#R222-01
Hieff® qPCR SYBR Green Master Mix	YEASEN	Cat#11201ES08
GentleMACSTM Dissociator	Miltenyibiotech	Cat#130-093-235

(Continued on next page)

Continued

REAGENT or RESOURCE	SOURCE	IDENTIFIER
Mini RNA isolation kit	Qiagen	Cat#74106
ChemiDoc MP Imaging System	Bio-Rad	Cat#12003154
Mouse CXCL2/MIP-2 ELISA Kit	MultiSciences	Cat#70-EK2142
PKH67 Green Fluorescent Cell Linker Mini Kit	Sigma-Aldrich	Cat#MINI67
Anti-F4/80-Microbeads UntraPure kit	Miltenyibiotech	Cat#130-110-443
Pan T cell isolation kit, human	Miltenyibiotech	Cat#130-094-538
MDSC Isolation Kit, mouse	Miltenyibiotech	Cat#130-094-538
Anti-Flag Magnetic Beads	Beyotime	Cat#P2115
Mouse IgG Magnetic Beads	Beyotime	Cat#P2171
Protein A/G Magnetic Beads	MedChemExpress	Cat#HY-K0202A
Deposited data		
TARGET data	TARGET	https://ocg.cancer.gov/programs/target
TCGA data	TCGA	https://portal.gdc.cancer.gov/
Raw mRNA expression data	This paper	GSE205440, GSE241824
Proteomics data	ProteomeXchange	PXD035216 PXD048589
Experimental models: Cell lines		
K7M2-WT	ATCC	Cat#CRL-2836
RAW 264.7	ATCC	Cat#TIB-71
HEK293T	ATCC	Cat#CRL-11268
Experimental models: Organisms/strains		
Mouse: Balb/c	Guangdong Medical Laboratory Animal Center	Cat#GDMLAC-03
Oligonucleotides		
RNAi sequences, see **Methods**	This paper	N/A
Primers for RT-qPCR, see Table S5	This paper	N/A
Recombinant DNA		
pCDH-CMV-MCS-EF1-Puro	System Biosciences	Cat#CD510B-1
pcDNA3-EGFP	Doug Golenbock (Addgene)	RRID: Addgene_13031
pLVX-Puro	Takara	Cat#632164
pCMV-Luc	Ralf Kuehn (Addgene)	RRID: Addgene_45968
Software and algorithms		
R	N/A	https://www.r-project.org
R Studio	N/A	https://www.rstudio.com/
NIH ImageJ1.51	NIH	N/A
GraphPad Prism 8.0a Software	GraphPad Software	N/A
flowjo_v10.8.1	Flowjo, L.L.C.	N/A
IVIS® Spectrum Living Image software	PerkinElmer	N/A
Carl Zeiss sofware	ZEISS	N/A
Pheatmap	R Core Team, 2016	https://cran.r-project.org/web/packages/pheatmap/index.html
Ggsurvplot (ggplot2)	Alboukadel Kassamnara	https://www.rdocumentation.org/packages/survminer/versions/0.4.6
DEseq2 (v1.6.3)	Love et al.[58]	https://bioconductor.org/packages/release/bioc/html/DESeq2.html
ClusterProfiler R package (v4.2.0)	Yu et al.[59]	N/A
GSEA (v4.2.3)	Broad Institute	https://www.broad.mit.edu/GSEA

RESOURCE AVAILABILITY

Lead contact

Further information and requests for resources and reagents should be directed to and will be fulfilled by the lead contact, Jin Wang (wangjinr@sysucc.org.cn).

Materials availability

Plasmids, cell lines, and materials are available to investigators at non-profit institutions upon the establishment of a material transfer agreement. Reagent sharing with investigators at for-profit institutions will be implemented after a licensing agreement.

Data and code availability

- Microarray gene expression data of murine macrophages exhibiting polarization toward M1, M2 and M2b were obtained from GEO under the accession number GSE69607 and GSE32690. Expression data and survival outcomes of candidate genes were obtained from GEO under the accession number GSE21257. Raw mRNA expression data of BMDMs treated with PBS or K7M2-EVs were deposited at the GEO under accession number GSE205440. Raw mRNA expression data of normal and pre-metastatic lungs were deposited at the GEO under accession number GSE241824. Proteomics data of EV-proteins and S100A11-interacting proteins have been deposited at ProteomeXchange database under accession number PXD035216 and PXD048589 respectively. The authenticity of this article has been validated by uploading the key raw data onto the Research Data Deposit public platform (www.researchdata.org.cn), with the approval number RDDB2024519699.
- This paper does not report original code.
- Any additional information required to reanalyze the data reported in this work paper is available from the lead contact upon request.

EXPERIMENTAL MODEL AND SUBJECT DETAILS

The antibodies used for IHC/IF, western blot and flow cytometry are listed in the Key Resources Table. The primers used for RT–qPCR are listed in the Table S5.

Cell culture

The BABL/C mouse osteosarcoma-derived cell line K7 was kindly provided by Prof. Yingqi Hua (School of Medicine, Shanghai Jiao Tong University, China). K7M2, the lung metastatic derivative of K7, and mouse macrophage cell line Raw264.7 were purchased from Zhong Qiao Xin Zhou Biotechnology Co., Ltd. (Shanghai, China). Cells were routinely cultured in DMEM with 10% fetal bovine serum (FBS) and penicillin/streptomycin in a humidified 37°C incubator with 5% CO_2. Cells were routinely tested negative for mycoplasma contamination. For EV isolation from culture supernatants, cells were changed to medium with EV-depleted FBS as previously reported.[21,60] To obtain bone marrow-derived macrophages (BMDMs), bone marrow cells were flushed out from the femurs and tibias of 5 to 8-week-old BALB/C mice. After red blood cell lysis and filtration, cells were cultured in RPMI 1640 supplemented with 10% heat-inactivated FBS and M-CSF (25 ng/mL) for 6 days.

Animal studies

All *in vivo* experiments on mice were approved by the Animal Research Committee of Sun Yat-sen University Cancer Center (NO. 17110D). Female BALB/C mice (4 weeks old) were obtained from Guangdong Medical Laboratory Animal Center. An *in vivo* ortho-topic osteosarcoma metastasis model was established as previously described.[61] Briefly, 1×10^6 osteosarcoma cells suspended in 10 μL PBS were injected into the proximal tibia. Lung metastasis was monitored by IVIS Lumina II (PerkinElmer). The number of lung metastases was determined by hematoxylin and eosin staining.

For *in vivo* depletion of macrophages, clodronate liposomes (200 μL/mouse, once per week, Yeasen Biotechnology) were IV injected. The depletion efficiency was validated by flow cytometry.

For *in vivo* depletion of gMDSCs, anti-Ly6G or anti-Ly6C antibody (Bio X Cell, 200 μg per mouse) was injected intraperitoneally every other day, starting 3 days after orthotopic implantation of osteosarcoma cells. Mice were sacrificed in 4 weeks.

For adoptive transfer, on day 5, 7, 9, 11, 13 after orthotopic implantation of K7-luc, purified gMDSCs (5×10^5 cells) from the lung PMN of K7M2-bearing mice were transferred into recipient mice intravenously as previously described. Lung metastasis was monitored as described above.

For gMDSCs distribution, purified gMDSCs from the lung PMN of K7M2-bearing mice were labeled with XenoLight DiR (PerkinElmer). Labeled gMDSCs (5×10^5 cells) were injected into mice intravenously. Organs were harvested for *ex vivo* fluorescence imaging (IVIS Spectrum, PerkinElmer) at 24 h after injection.

For the lung colonization study, 5×10^5 K7M2 cells were injected into the proximal tibia. From the next day on, the mice received anti-Ly6g or anti-Ly6c antibody every other day. On day 13, 1×10^6 GFP-labeled K7M2 cells (K7M2-GFP) were injected via the tail vein. The mice were sacrificed, and the lungs were harvested for tumor cell colonization analysis by flow cytometry and immunofluorescence 24 h later.

For *in vivo* CXCL2 neutralizing experiment, on day 3 of orthotopic K7M2 implantation, isotype control or anti-CXCL2 antibody (Leinco, USA) were injected intraperitoneally diluted in PBS, 2 μg per mouse every 2 days, for a total 2 weeks. Mice were sacrificed in 4 weeks.

EVs isolation

EVs from cell lines were isolated by ultracentrifugation as described previously.[21,60] Briefly, the cell culture supernatant was collected and centrifuged at 2000 × g for 10 min and then at 10,000 × g for 30 min. The supernatant was passed through a 0.22 μm filter and then ultracentrifuged at 100,000 × g for 2 h. The pellet was resuspended in PBS and re-ultracentrifuged at 100,000 × g for 2 h. The EV pellet was resuspended in PBS and used immediately or stored at −80°C. The morphology of EVs was imaged by transmission electron microscopy, and the size was analyzed by a Nanosight NS300 (Malvern Instruments). The concentration of EVs was measured by a BCA assay (CWBIO, China).

EVs application

For labeling, EVs were fluorescently stained using PKH67 (Sigma) or XenoLight DiR (PerkinElmer) and then washed through exosome spin columns (MW3000, Invitrogen) as described by Chen et al.[62] Labeled EVs (20 μg) were injected into mice intravenously. Organs were harvested for flow cytometry, immunofluorescence, and *ex vivo* fluorescence imaging (IVIS Spectrum, PerkinElmer) at 24 h after EV injection.

For the visualization of EVs internalization, labeled EVs (5 μg) were added to primary BMDMs, F4/80^{−} cells or F4/80[+] macrophages sorted by anti-F4/80-Microbeads UntraPure kit (Miltenyi Biotech) from mouse lung for 24 h. Cells were then fixed with 4% paraformaldehyde in PBS for 10 min at room temperature (RT). After permeabilizing with 0.5% Triton X-100 for 5 min, cells were incubated with 100 nM TRITC Phalloidin (Yeasen Biotechnology) for 30 min at RT. Then, cells were washed and counterstained with DAPI (Sigma-Aldrich). Images were obtained and analyzed with confocal microscope (LSM880, Zeiss).

For *in vivo* EVs education, 10 μg of EVs in 100 μL of PBS was injected via tail vein every 3 days for 2 weeks. Tumor cells were then injected intravenously via mouse tail vein.

Immunohistochemistry (IHC) and immunofluorescence (IF)

IHC was carried out on 4-μm sections from FFPE tissues on a Ventana Discovery XT automated system (Ventana Medical Systems). Immunoreactive score of S100A11 was calculated as previously described.[63] Staining intensity of cytoplasm and membrane was scored as 0: negative, 1: weak, 2: moderate or 3: strong. The percentage of staining was categorized as 0: no staining, 1: 1–10% of stained cells, 2: 11–50% of stained cells, 3: 51–80% of stained cells, and 4: 81–100% of stained cells. The final staining score was defined as proportion multiply intensity score. The median score was used as the cutoff value to classify osteosarcoma patients into a higher (>median) or lower (≤median) expressing group.

IF was performed on cryosections of lung tissue. Briefly, freshly dissected lungs were immediately embedded and frozen in Tissue-Tek OCT (SAKURA). Lung cryosections were blocked with 5% BSA for 60 min and then incubated with a conjugated primary antibody overnight at 4°C. After washing with PBS, the sections were mounted with ProLong Diamond Antifade Mountant with DAPI (Invitrogen). Images were obtained and analyzed with a confocal microscope (LSM880, Zeiss). The antibodies are listed in the Key Resources Table.

Flow cytometry analysis of infiltrated immune cells

Lungs of tumor-bearing mice were lavaged with normal saline and then cut into small pieces. Tissues were homogenized using a gentleMACS dissociator (Miltenyi Biotec) in solution with 2 mg/mL collagenase type I (Sigma), 2 mg/mL collagenase type IV (Sigma), and 1 mg/mL DNase (Sigma). The suspension was filtered through a 70-μm cell strainer. For analysis of spleen immune cells, the spleen was smashed through a 70-μm nylon mesh in 1640 medium. Cell suspensions were lysed in RBC lysis buffer (Biolegend) to remove RBCs and then washed, counted, and resuspended in PBS. Suspensions were first blocked with Fc-block (CD16/CD32) and then incubated with the indicated primary antibodies for 30 min at room temperature. After washing with PBS twice, the cells were analyzed by a CytoFLEX (Beckman Coulter). Gating was determined by the fluorescence minus one approach. Data were analyzed with CytExpert V2.4 or FlowJo V10 software. The antibodies used for flow cytometry are listed in the Key Resources Table.

Flow cytometry of human samples

Informed consent was obtained from all patients in the study. The Institutional Review Board of Sun Yat-Sen University Cancer Center approved this study. Peripheral blood was collected and processed within 4 h. The blood was centrifuged at 800 g without braking for 8 min. The buffy coat in the middle layer was gently collected and lysed in RBC lysis buffer and then washed twice with PBS. The cells were suspended in heat-inactivated FBS with 10% dimethylsulfoxide and then transferred to −80°C overnight before long-term storage in liquid nitrogen. When recovered, the frozen cells were rapidly thawed at 37°C and then gently washed with PBS twice before proceeding to antibody incubation and flow cytometry analysis.

Granulocytic MDSCs isolation

Granulocytic MDSCs were isolated from the lung or spleen of K7M2-bearing mice in 2 weeks using an MDSC Isolation Kit (Miltenyi Biotec). Briefly, the lung and spleen were processed the same as for flow cytometry analysis. The suspension was passed through

30 μm nylon mesh to remove cell clumps. Then, positive selection of gMDSCs was conducted according to the manufacturer's protocol. The purity of harvested CD11b$^+$Ly6G^{high} cells was more than 95% confirmed by flow cytometry analysis. GMDSCs were resuspended in RPMI 1640 with 10% heat-inactivated FBS for further experiments.

In vitro T cell suppression assay

Granulocytic MDSCs (Ly-6G$^+$) were isolated from the lungs of K7M2 tumor-bearing mice as mentioned above. CD3$^+$ T cells were isolated from the spleens of the same mice using a pan-T-cell Isolation Kit (Miltenyi Biotec) and then labeled with 0.5 μM carboxyfluorescein succinimidyl ester (CFSE, Invitrogen). A 96-well U-bottom plate was precoated with anti-mouse CD3 antibody (4 μg/mL, Biogems) overnight at 4°C. Granulocytic MDSCs (1 × 10^5) were cocultured with CD3$^+$ T cells at different ratios of 1:1 and 1:4 in RPMI 1640 with 10% heat-inactivated FBS containing anti-mouse CD28 antibody (2 μg/mL, Biogems) and mouse IL-2 (50 ng/mL, Peprotech). The control group was activated T cells alone. The proliferation of T cells was analyzed by flow cytometry after inoculation for 48 h.

Plasmids, cloning and lentivirus production

To generate stable knockdown cell lines, shRNAs against murine Rab27a and S100a11 were inserted into the pLVX-shRNA2-Luc-Puro vector. The shRNAs used were as follows: Rab27a shRNA: CCGGGCTTCTGTTCGACCTGACAAACTCGAGTTTGTCAGGTCG AACAGAAGCTTTTTG, S100a11 shRNA: GGATCCGCACACCTACCACAACATGTACTCGAGTACATGTTGTGGTAGGTGTGCTTTTT TGAATTC. Lentivirus packing murine S100A11-expression vectors (pCDH-EF1-Puro) were obtained from Synbio Tech. (Suzhou, China). Lentivirus was produced in 293T cells. Cells were infected with viral particles and selected by the indicated concentration of puromycin for 7 days.

The expression vectors containing S100A11 or Flag-tagged S100A11 were purchased from Synbio Tech. (Suzhou, China). 293T cells were transfected with Lipofectamine 3000, while Raw264.7 cells were transfected with Advanced DNA RNA Transfection Reagent (Zeta Life, USA) according to the manufacturer's instructions.

RNAi-mediated silencing

For siRNA transfection, Raw264.7 cells were transfected with 100 nM control siNC or siRNA targeting mouse USP9x using Advanced DNA RNA Transfection Reagent (Zeta Life, USA). The transfected cells were harvested for analysis or further procedures after 48h. The siRNA sequences targeting USP9x were listed as follows: siUSP9x-1: F-GCUUAACUUUCUUAGGUUUTT, R-AAACCUAAGAAA GUUAAGCCG. SiUSP9x-2: F-AGAAGAAAUCACUAUGAUUTT, R-AAUCAUAGUGAUUUCUUCUGC.

Immunoprecipitation-mass spectrometry (IP-MS) analysis

S100A11 pull-down assay was performed and optimized using a manual immunoprecipitation for FLAG-labeled protein interaction. Briefly, FLAG-tagged S100A11-overexpressing HEK-293T cells were extracted and lysed in Pierce IP Lysis Buffer (Thermo, USA) containing 1× protease inhibitor cocktail and phosphatase inhibitor cocktail (Bimake, China). The protein complex was then incubated with pre-washing BeyoMag Anti-Flag Magnetic Beads (Beyotime, China) or Mouse IgG Magnetic Beads (Beyotime, China) overnight at 4°C with mixing. Subsequently, the protein-beads complex was separated and collected by a DynaMag-2 Magnet (Thermo, USA) followed by the antigen recovery with 1× SDS-PAGE loading buffer for 5 min boiling. The S100A11-specific binding proteins were analyzed by gradient gel electrophoresis followed by Coomassie brilliant blue staining (Beyotime, China). The specific band was identified by liquid chromatography combined with mass spectrometry (LC-MS) at Wininovate Bio. Co. Ltd. (Shenzhen, China).

Coimmunoprecipitation (Co-IP)

Protein was extracted from Raw264.7 cells as mentioned above. Antibody against USP9X or rabbit IgG was added to the lysates and incubated overnight at 4°C with mixing. Next, the protein-antibody complex was then incubated with the pre-washing Protein A/G Magnetic Beads (MCE, USA) for 1 h at room temperature. The beads were then washed and collected by a DynaMag-2 Magnet (Thermo). Bound protein was eluted with 1× loading buffer with boiling at 95°C–100°C for 5 min, and then resolved by 10% SDS–PAGE followed by Western blotting with an anti-S100A11 antibody.

Western blot (WB) analysis

Briefly, cells or EVs were lysed in RIPA buffer (CWBIO, China) containing protease inhibitor and phosphatase inhibitor (Selleck, China). Protein was separated by SDS–PAGE and then transferred to PVDF membranes (Millipore). After blocking with 5% nonfat milk, the membranes were probed with the indicated primary antibody overnight at 4°C and then incubated with the corresponding secondary antibodies. Bands were detected by Chemidoc Touch (Bio–Rad) with Clarity Western ECL substrate (Bio–Rad). The antibodies are listed in the Key Resources Table.

Reverse transcription PCR and real-time quantitative PCR

Total RNA from cells or tissues was prepared using TRIzol reagent, and cDNA was synthesized with HiScript II Q RT SuperMix (Vazyme). PCR amplification was performed with 0.5 μL of the cDNA, specific primers and Taq DNA Polymerase (Takara

Bio Inc.). PCR products were separated by gel electrophoresis. The primers used for RT–PCR detection of luciferase were as follows: Luciferase-F: 5′-TGGGCGCGTTATTTATCGGA-3′, Luciferase-R: 5′-CGGTTTATCATCCCCCTCGG-3′, Gapdh-F: AGGTCGGTGTGA ACGGATTTG, Gapdh-R: TGTAGACCATGTAGTTGAGGTCA. Real-time quantitative PCR (RT–qPCR) was performed at BIO-RAD CFX96 with Hieff qPCR SYBR Green Master Mix (Yeasen Biotechnology). The primers used for RT–qPCR are listed in the Table S5.

ELISA
The medium was collected from cell cultures and processed according to the manufacturer's instructions (Multi Science) for the detection of murine CXCL2.

Chemotaxis assay
Conditioned medium or RPMI 1640 added with recombinant murine CXCL2 was placed in the lower chamber of a 24-well Transwell system (5 μm, BD Falcon). A total of 1×10^6 gMDSCs isolated from the spleens of tumor-bearing mice were seeded in the upper chamber. Migrated cells in the lower chamber were counted by Countstar (Countstar). For treatment with SB225002, BP-1-102 or fedratinib (Selleck, China), the indicated doses of reagents were added to the upper chamber.

RNA sequencing (RNA-seq)
RNA-seq was performed by Sinotech Genomics Co. Ltd. (Shenzhen, China) using Illumina NovaSeq 600 according to the manufacturer's instruction. Approximately 6 GB clean data per sample were collected for analysis. The RNA-Seq data can be assessed in the GEO database via accession number GSE205440 and GSE241824.

Gene set enrichment analysis (GSEA)
GSEA was conducted using GSEA2.2.4 software in Hallmark C7.all datasets with default settings. To obtain the specific gene signature of M1, M2 and M2b macrophages, we used the Gene Expression Omnibus (GEO) databases GSE69607 and GSE32690 to obtain the RNA expression profile of M0, M1 and M2b, and identified the differentially expressed genes of M1 vs. M0, M2 vs. M0 and M2b vs. M0, respectively. Up-regulated genes were screened according to the limma R package (v 3.50.0, fold change >2, FDR <0.05) and imported into GSEA (v4.2.3, https://www.broad.mit.edu/GSEA) software for gene sets. GSEA of each hub gene with the RNA sequence data was performed.

Mass spectrometry (MS)
The protein cargos carried by EVs from K7 and K7M2 cells were analyzed by LC–MS at Wininovate (Shenzhen, China). The obtained data were analyzed for protein identification and quantification using Proteome Discoverer. The local false discovery rate was 1.0% after searching against the *Mus musculus* sequence with a maximum of two missed cleavages and one missed terminus cleavage. The following settings were selected: oxidation (M), acetylation (protein N-term), deamidation (NQ), pyro-glu from E, pyro-glu from Q for variable modifications and carbamidomethylation (C) for fixed modifications. The precursor and fragment mass tolerances were set to 10 ppm and 0.05 Da, respectively.

QUANTIFICATION AND STATISTICAL ANALYSIS

The data are presented as the mean ± standard deviation (SD) from at least 3 independent experiments. Statistical analyses were carried out in GraphPad Prism 8 (Version 8.4.0, San Diego, CA, USA). Student's t test or one-way ANOVA with a Bonferroni post hoc test was used to determine the significance of differences among groups. Kaplan–Meier survival curves and log rank tests were used to evaluate overall survival in mice and lung metastasis-free survival in osteosarcoma patients. Cox proportional hazards model was used for multivariate survival analyses using SPSS 20.0. ns: non-significant, *$p < 0.05$, **$p < 0.01$, ***$p < 0.001$, ****$p < 0.0001$.